Supporting Information for "Experimental and theoretical exploration of bismuth oxyhalides (BiOX, X = Cl, Br, I) nanoparticles in thermoelectric, optoelectronic, and photocatalytic applications"

Imran Hossain Sabuj,[1] Quazi Shafayat Hossain,[1] Sadiq Shahriyar Nishat,[2] Shirin Akter Jahan,[3] M. N. I. Khan,[4] Umme Sarmeen Akhtar,[3] Muhammad Shahriar Bashar,[5] Dipa Islam,[6] Md. Zakir Sultan,[7] Sharmin Jahan,[8] Khandker Saadat Hossain,[9] Sazzad M. S. Imran,[1] and Imtiaz Ahmed[1,*]

[1] *Materials Science Research Laboratory, Department of Electrical and Electronic Engineering, University of Dhaka, Dhaka-1000, Bangladesh*
[2] *Department of Materials Science and Engineering, Rensselaer Polytechnic Institute, Troy, New York 12180, United States*
[3] *Institute of Glass and Ceramic Research and Testing, Bangladesh Council of Scientific and Industrial Research, Dhaka-1205, Bangladesh*
[4] *Materials Science Division, Atomic Energy Centre, Dhaka-1000, Bangladesh*
[5] *Institute of Energy Research and Development, Bangladesh Council of Scientific and Industrial Research, Dhaka-1205, Bangladesh*
[6] *Biomedical and Toxicological Research Institute, Bangladesh Council of Scientific and Industrial Research, Dhaka-1205, Bangladesh*
[7] *Centre for Advanced Research in Sciences, University of Dhaka, Dhaka-1000, Bangladesh*
[8] *Institute of Food Science and Technology, Bangladesh Council of Scientific and Industrial Research, Dhaka-1205, Bangladesh*
[9] *Nanophysics and Soft Matter Laboratory, Department of Physics, University of Dhaka, Dhaka-1000, Bangladesh*

[*] imtiaz@du.ac.bd

I. COMPUTATIONAL METHODS

The projector-augmented wave (PAW) derived core-valence interactions facilitated the spin-polarized DFT simulations in Vienna *Ab Initio* Simulation Package VASP 6.4.2 code [1–3]. The unit cells of BiOX (Fig. S3) consist of Bi (2), O (2), and X (2) atoms. Unless stated otherwise, $2\times2\times2$ supercells consisting of 48 atoms were considered for all simulations presented here. The 15 electrons in Bi ($5d^{10}6s^26p^3$), 6 electrons of O ($2s^22p^4$), 7 electrons of Cl ($3s^23p^5$), 7 electrons of Br ($4s^24p^5$), and 7 electrons of I ($5s^25p^5$) were considered as valence in PAW, treating the remaining electrons as core. During relaxations, the threshold for self-consistent electronic and Hellmann-Feynman ionic convergences were set to 10^{-8} eV/atom and 10^{-4} eV/Å, respectively. The electronic eigenstates were represented by a plane wave expansion with an energy cutoff of 580 eV. The $13 \times 13 \times 9$ Monkhorst-Pack (MP) k-mesh was used to perform Brillouin zone (BZ) integrations.

The DFT computational accuracies depend on the complexity of XCFs used to model the unknown electronic interaction [4, 5]. Different XCFs like local density approximation (LDA), GGA-PBE, GGA-PBE for solid (GGA-PBEsol), and Hubbard interaction-corrected DFT+U_d+U_p were implemented [6–13]. The long-range van der Waals (vdW) correction with Becke-Johnson (BJ) damping at DFT-D3 level was invoked [14]. The spin-orbit coupling (SOC) effect was considered to incorporate relativistic effects of the heavy Bi atom [14]. The screened hybrid functional Heyd–Scuseria–Ernzerhof (HSE06) was implemented with Hartree-Fock (HF) exact-exchange mixing α_HF of 25% [15–22]. The vdW and SOC were combined with HSE06 as HSE06+SOC, HSE06+vdW, and HSE06+vdW+SOC. The PBE-HFα_HF% was implemented where the exchange-correlation (XC) energy $E_\mathrm{XC}^\mathrm{HSE}$ in terms of short-range (SR) and long-range (LR) components of the HSE-screened approach as

$$E_\mathrm{xc}^\mathrm{HSE} = \alpha_\mathrm{HF}E_\mathrm{x}^\mathrm{HF,SR}(\mu) + (1-\alpha_\mathrm{HF})E_\mathrm{x}^\mathrm{PBE,SR}(\mu) + E_\mathrm{x}^\mathrm{PBE,LR}(\mu) + E_\mathrm{c}^\mathrm{PBE}(\mu) \quad \text{(S1)}$$

where $\mu = 0.2$ Å^{-1} sets the standard screening level [16, 23–25]. The α_HF was tuned along with vdW and SOC to implement PBE-HF30%+vdW+SOC, PBE-HF21%+vdW+SOC, and PBE-HF22%+vdW+SOC.

The parabolic fitting of conduction band (CB) and valence band (VB) extrema of the

simulated electronic BS provided the carrier effective mass [26]. The carrier transport in terms of conductivity, mobility, Seebeck coefficient, and electronic contribution to thermal conductivity was characterized by solving Boltzmann transport equations from dense electronic DOS of PBE-HFα_{HF}%+vdW+SOC XCF and the Onsager coefficients in the BoltzTraP and AMSET codes [27, 28]. The constant relaxation time (CRT) approximation in BoltzTraP assumed a CRT of 1×10^{-15} s. The scattering from acoustic deformation potentials (ADPs), polar optical phonons (POPs), and ionized impurities (IMPs) were considered in AMSET codes. During lattice thermal conductivity estimation in Phono3py at DFT+U_{d}+U_{p} level, force constants (second and third order) were evaluated in a $4 \times 4 \times 4$ supercell with 0.03 Åsdisplacements. The self-consistent energy and force convergences were set to 1×10^{-4} eVÅ^{-1} and 1×10^{-8} eV [29, 30]. A dense Γ centered $21 \times 21 \times 21$ point mesh ensured the accuracy of the lattice thermal conductivities calculations. The harmonic phonon modes were examined with the density functional perturbation theory (DFPT) and a $4 \times 4 \times 4$ supercell based finite difference method using Phonopy 2.22.1 [29, 31–33]. The electronic DOS, BS, and complex dielectric constant derived optical properties were simulated at LDA, GGA-PBE, GGA-PBE+vdW, GGA-PBEsol, and GGA-PBEsol+vdW. The self-interaction error-prone band gap underestimation problem of these functionals was alleviated with DFT+U_{d}+U_{p} with adhoc $U_{\mathrm{d}} = 5$ and 10 eV on Bi-5d and $U_{\mathrm{p}} = 4$ and 5 eV on O-2p, Cl-3p, Br-3p, and I-5p. For accurate electronic and optical properties, sophisticated XCFs like HSE06, HSE06+vdW, HSE06+SOC, HSE06+vdW+SOC, and PBE-HFα_{HF}%+vdW+SOC were invoked. The convergence of computationally intense hybrid XCFs-based BS simulations were ensured by Wannier interpolation implemented in the WANNIER90 tool [16, 34–36].

The Raman tensor simulation at LDA, GGA-PBE, and GGA-PBEsol levels were carried out in QUANTUM-ESPRESSO (QE 7.5) code [37–39]. The self-consistent relaxations were subjected to 10^{-8} eV/atom, 10^{-4} eV/Å, 580 eV, and $9 \times 9 \times 9$ for electronic, force convergences, plane wave cutoff, and MP k-mesh, respectively. The finite difference method (0.01 Å atomic displacement) based derivative of the dielectric tensor yields the Raman tensor in `dynmat.x` code.

II. MATERIALS SYNTHESIS

BiOCl. In the beginning, 5 mmol (2.2903 g) $Bi(NO_3)_3.5H_2O$ (99+% pure, Sigma) was added in 7.5 mL acetic acid (100% pure, Sigma). After the complete dissolution of $Bi(NO_3)_3.5H_2O$, 60 mL methanol was mixed in the solution with 30 min of constant magnetic stirring (700 rpm). Subsequently, a white suspension was formed in the solution as 8.4 mL of 0.6M HCl (37% w/w, Sigma) was added dropwise into it. The pH was set to 5 by adding NH_4OH (25% w/w, Sigma) and the resulting white cloudy solution was stirred for 30 min before loading into a Teflon-lined reactor inside a stainless steel autoclave to react at 180 °C for 5 h inside an oven. After cooling down to room temperature, the white precipitate obtained from the reactor was washed several times with nanowater (18 MΩ, 7000 rpm, 6 cycles) and ethanol (7000 rpm, 6 cycles) and dried in air at 60 °C for 12 h to produce the final BiOCl sample.

BiOBr. At first, 10 mmol (4.8507 g) $Bi(NO_3)_3.5H_2O$ and 10 mmol (1.19 g) of KBr (99+% pure, Sigma) were completely dissolved in 70 mL of 0.1M HNO_3 (A) and 12 mL nanowater (B), respectively by vigorous magnetic stirring (650 rpm) for 45 min. The aqueous B solution was added dropwise into the A solution slowly and the resulting white mixture was subjected to constant magnetic stirring for 1 h. The pH of this white solution was 1 and subsequently transferred into the autoclave for hydrothermal reaction at 160 °C for 12 h inside an oven. Following the natural cooling to ambient temperature, higher speed centrifugation (7000 rpm) with nanowater (5 cycles) and ethanol (5 cycles) removed the residual ions from the precipitate before being subjected to drying in air for 12 h. The dried white BiOBr powder is used for further characterization.

BiOI. Initially, 4 mmol (1.9403 g) $Bi(NO_3)_3.5H_2O$ was finely dissolved into 40 ml of absolute ethanol (99+% pure, Sigma) through vigorous magnetic stirring and ultrasonication (A). Next, 4 mmol (0.664 gm) KI (99+% pure, Sigma) was dissolved in 30 ml of nanowater (B). Solution B was added dropwise into A under continuous stirring. The mixture turned white with pH=1 and was gradually brought to pH = 8.8 by adding NH_4OH. During the pH adjustment, the white color turned brick red close to pH 7. The solution was heated to 70 °C for 3 h. After natural cooling to room temperature, the dark red precipitate was collected and subsequently washed in nanowater and ethanol. The red powder was dried at 80 °C for 24 h, and used as the final BiOI powder.

III. PHOTOCATALYTIC SAMPLE PREPARATION

The RhB dye with a 10 ppm concentration was dissolved into 100 mL of nanowater. The BiOX (X = Cl, Br, I) photocatalyst concentration was set to 1 g/L. The solution pH was brought to 10 by adding the required NH_4OH. The adsorption-desorption equilibrium was attained with vigorous magnetic stirring in dark conditions for 60 min. During the optical exposure, constant magnetic stirring eliminated the RhB dye concentration gradients capable of inducing spurious catalytic effects. Depending on the reaction rate, UV-vis absorption measurements were taken in 10 (BiOCL), 15 (BiOBr), and 30 (BiOI) min intervals.

IV. CHARACTERIZATION TECHNIQUES

The crystallographic information was obtained from powdered X-ray Diffraction (XRD) measurements over angular range of 10° to 80° (Rigaku SmartLab SE Multipurpose, accelerating voltage 40 kV and tube current 40 mA, Cu Kα λ = 0.15418 nm X-ray source, step size 0.02° and scan speed 2°/min). The Raman spectra were recorded using a 532 nm laser excitation by LabRAM HR Evolution Confocal Raman Microscope from Horiba Scientific. The infrared absorptions were measured in a PerkinElmer Fourier Transform Infrared (FTIR) spectrometer. The surface morphology, elemental and purity analysis were facilitated in a Field Emission Scanning Electron Microscope (FESEM, JEOL 7610F) coupled with an Energy Dispersive X-ray (EDX) spectrometer (JED 2300) and SEM from AVO Research with EDX (EDAX Team). The chemical state analysis were performed with X-ray Photoelectron Spectrometer (XPS, Thermo Fischer Scientific, 1486.69 eV Al Kα source operating at 225 W). The C-1s XPS peak was adjusted to 284.8 eV for binding energy calibration. The Shimadzu UV-2600i UV–vis–NIR Spectrometer coupled with an integrating sphere was used to perform diffuse reflectance spectroscopy (DRS). The room temperature steady-state photoluminescence (PL) spectra were measured with Hitachi F-7000 Fluorescence Spectrophotometer (150 W Xe lamp and photomultiplier tube operating at 700 V). The UV-vis absorptions in photocatalytic degradation measurements were obtained by a Shimadzu UV-1900i spectrometer.

V. CRYSTALLOGRAPHIC INFORMATION

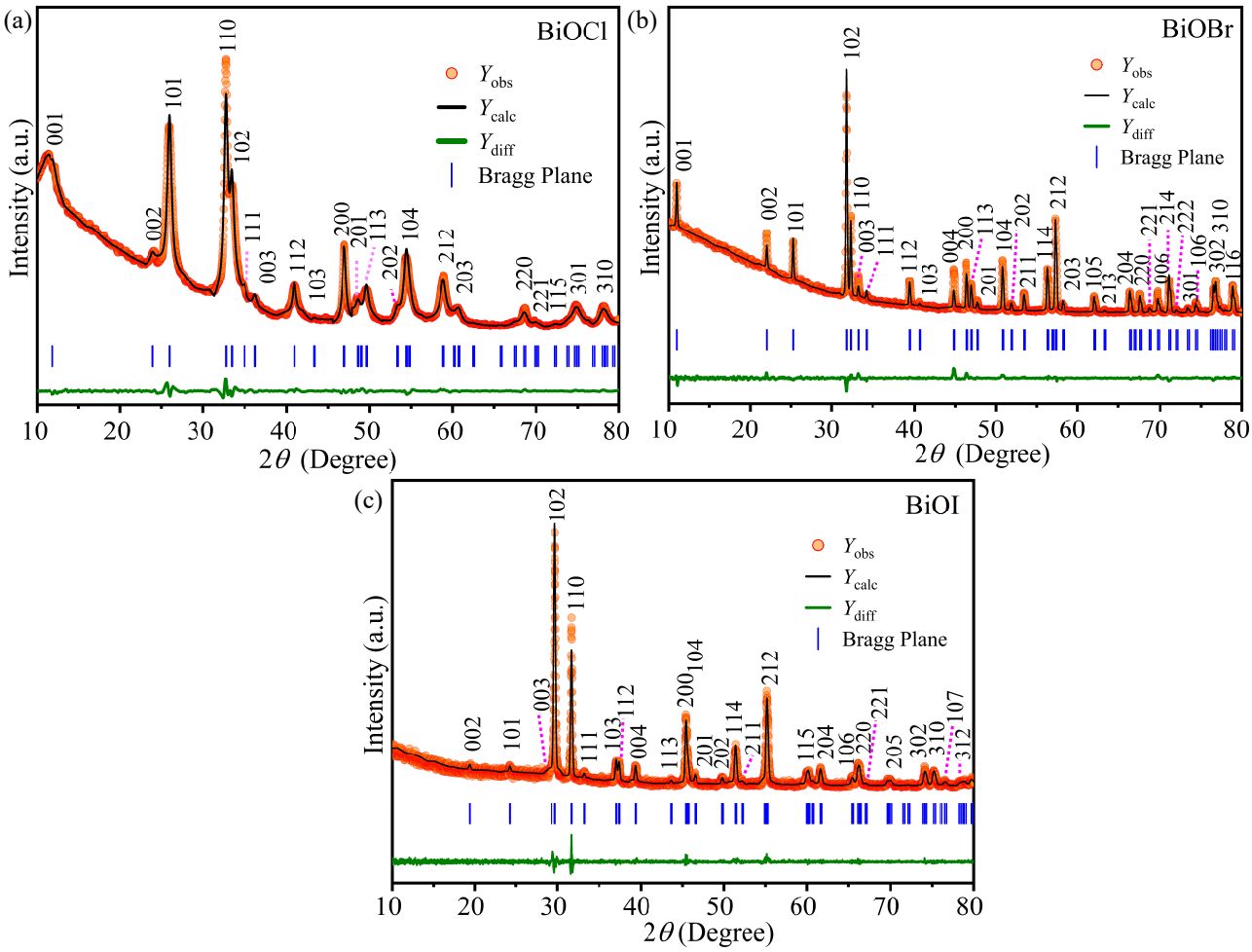

FIG. S1. Powder XRD data with Rietveld refinement for (a) BiOCl, (b) BiOBr, and (c) BiOI. The experimental data Y_{obs} were marked with yellow circles, refined patterns Y_{calc} were denoted by the black solid line, and the bottom green curve represented the difference between Y_{obs} and Y_{calc}.

VI. ENERGY VERSUS VOLUME ANALYSIS

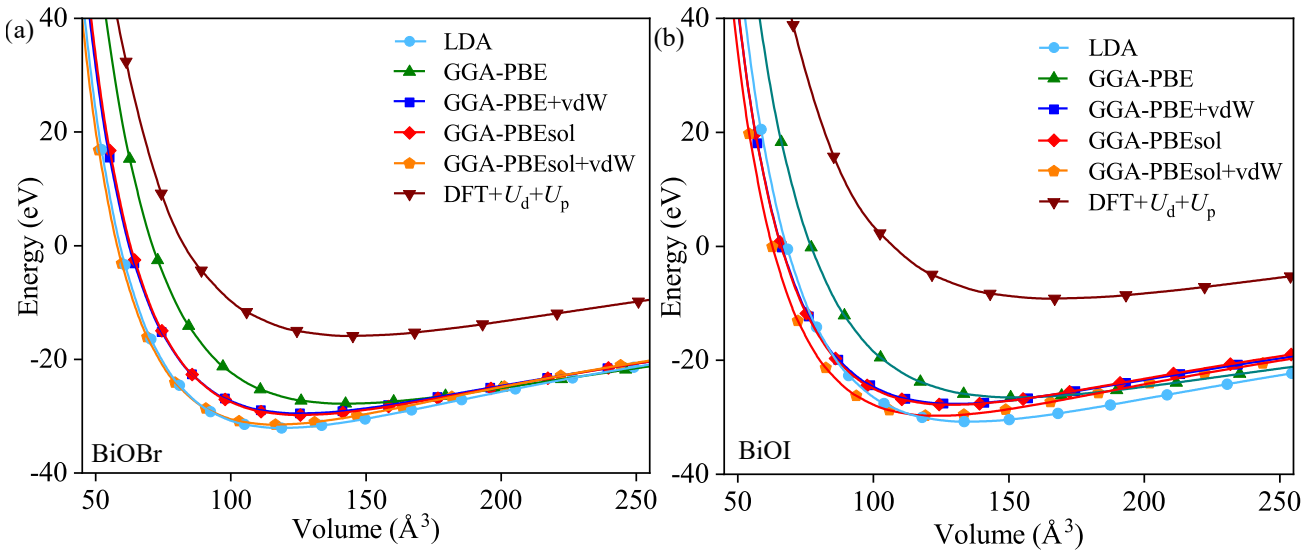

FIG. S2. Energy E versus volume V curve of (a) BiOBr, and (b) BiOI for different DFT exchange-correlation functionals (XCFs).

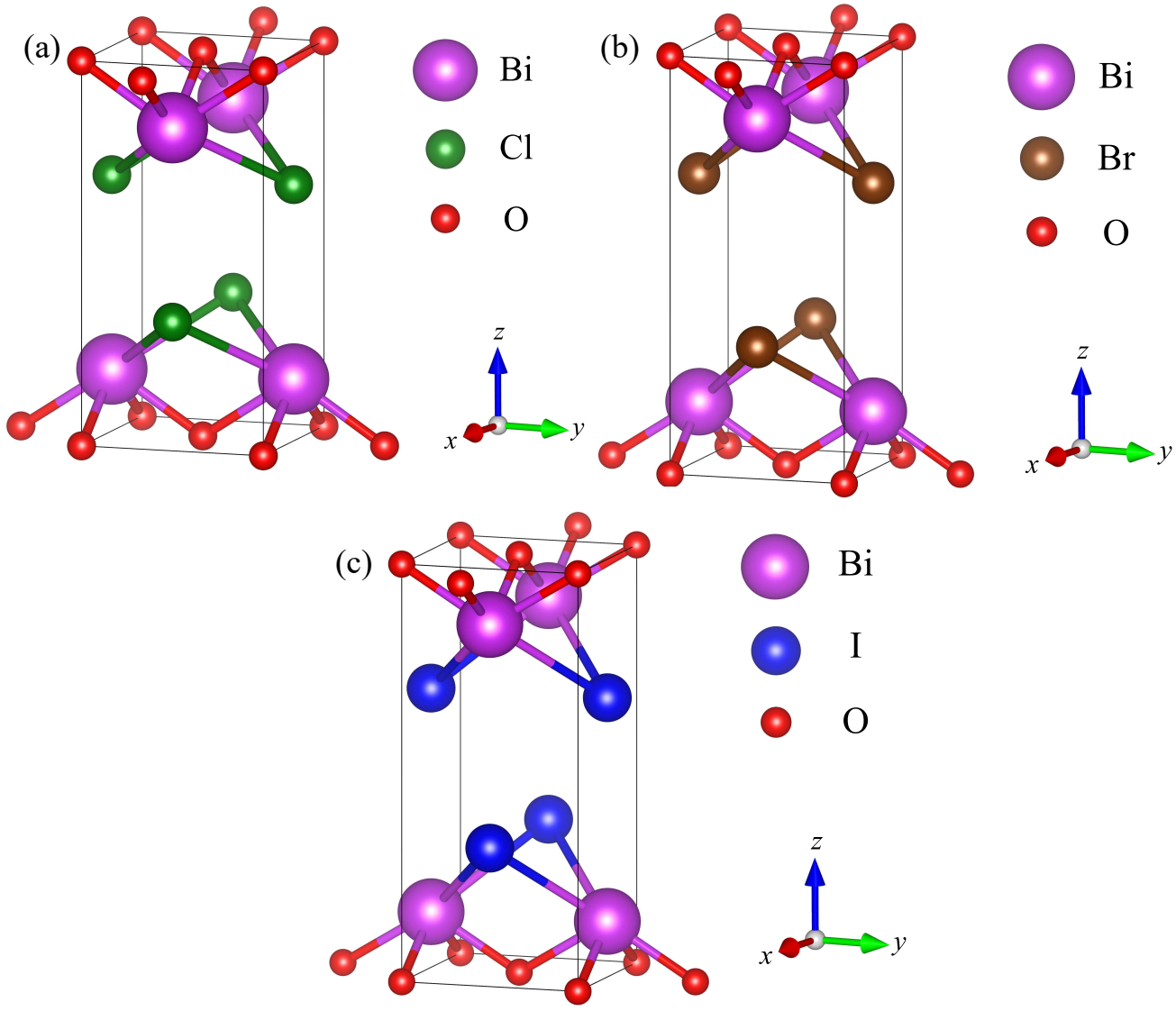

FIG. S3. Unit cell of (a) BiOCl, (b) BiOBr, and (c) BiOI consisting of 6 atoms: Bi (2), O (2), and X (2).

TABLE S1. Experimental (Exp.), LDA, GGA-PBE, GGA-PBE+vdW, GGA-PBEsol, GGA-PBEsol+vdW, and DFT+U_{d}+U_{p} relaxed crystallographic parameters with bulk modulus B_0 and its first pressure derivative B_0' of BiOCl. R.F. = Rietveld Factor: R_{p}=4.16%, R_{wp}=5.78%, R_{exp}=3.79%, Hubbard Corrections: $U_{\mathrm{p}} = 5$ eV on O-2p & Cl-3p, $U_{\mathrm{d}} = 10$ eV on Bi-5d.

Crystallographic Parameters													
Sample	a (Å)	b (Å)	c (Å)	$d_{\mathrm{Bi\text{-}O}}$ (Å)	$d_{\mathrm{Bi\text{-}Cl}}$ (Å)	B_0(GPa)	B_0'	α(°)	β(°)	γ(°)	V_0 (Å^3)	E_0 (eV)	R.F.
BiOCl (Exp.)	3.8701(3)	3.8701(2)	7.4349(1)	2.335(×4)	3.129(×4)	–	–	90	90	90	111.3575(2)	–	χ^2=2.33
LDA	3.8558	3.8558	7.1580	2.301(×4)	3.017(×4)	101.9	3.95	90	90	90	106.4185	−33.584	–
GGA-PBE	3.9135	3.9135	7.9609	2.338(×4)	3.094(×4)	78.7	3.95	90	90	90	121.9262	−29.351	–
GGA-PBE+vdW	3.9069	3.9069	7.3268	2.331(×4)	3.064(×4)	88.2	3.97	90	90	90	111.8384	−30.904	–
GGA-PBEsol	3.8805	3.8805	7.3410	2.315(×4)	3.043(×4)	92.8	3.96	90	90	90	110.5425	−31.250	–
GGA-PBEsol+vdW	3.8610	3.8610	7.1085	2.306(×4)	3.017(×4)	99.6	3.96	90	90	90	105.9719	−32.797	–
DFT+U_{d}+U_{p}	4.0192	4.0192	7.4221	2.374(×4)	3.150(×4)	83.44	4.21	90	90	90	119.8985	−9.19	–

TABLE S2. Experimental (Exp.), LDA, GGA-PBE, GGA-PBE+vdW, GGA-PBEsol, GGA-PBEsol+vdW, and DFT+U_{d}+U_{p} relaxed crystallographic parameters with bulk modulus B_0 and its first pressure derivative B_0' of BiOBr. R.F. = Rietveld Factor: R_{p}=5.88%, R_{wp}=5.65%, R_{exp}=3.97%. Hubbard Correction: $U_{\mathrm{p}} = 3$ eV on O-2p & Br-4p, $U_{\mathrm{d}} = 5$ eV on Bi-5d.

Crystallographic Parameters													
Sample	a (Å)	b (Å)	c (Å)	$d_{\mathrm{Bi\text{-}O}}$ (Å)	$d_{\mathrm{Bi\text{-}Br}}$ (Å)	B_0(GPa)	B_0'	α(°)	β(°)	γ(°)	V_0 (Å^3)	E_0 (eV)	R.F.
BiOBr (Exp.)	3.9183(1)	3.9183(2)	8.0898(1)	2.322(×4)	3.164(×4)	–	–	90	90	90	124.2033(2)	–	χ^2=2.12
LDA	3.8897	3.8897	7.8505	2.310(×4)	3.132(×4)	91.4	4.00	90	90	90	118.7782	−32.487	–
GGA-PBE	3.9498	3.9498	9.1326	2.347(×4)	3.223(×4)	66.9	3.99	90	90	90	142.4392	−28.257	–
GGA-PBE+vdW	3.9360	3.9360	8.1073	2.339(×4)	3.183(×4)	79.4	4.00	90	90	90	125.6042	−29.971	–
GGA-PBEsol	3.9074	3.9074	8.2379	2.323(×4)	3.163(×4)	81.7	4.00	90	90	90	125.7778	−30.240	–
GGA-PBEsol+vdW	3.8992	3.8992	7.6636	2.316(×4)	3.126(×4)	91.5	4.01	90	90	90	116.5150	−31.896	–
DFT+U_{d}+U_{p}	3.9908	3.9908	9.1134	2.363(×4)	3.251(×4)	67.4	4.26	90	90	90	145.1494	−15.84	–

TABLE S3. Experimental (Exp.), LDA, GGA-PBE, GGA-PBE+vdW, GGA-PBEsol, GGA-PBEsol+vdW, and DFT+U_{d}+U_{p} relaxed crystallographic parameters with bulk modulus B_0 and its first pressure derivative B_0' of BiOI. R.F. = Rietveld Factor: R_{p}=10.35%, R_{wp}=9.28%, R_{exp}=5.25%. Hubbard Correction: $U_{\mathrm{p}} = 4$ eV on O-2p & I-5p, $U_{\mathrm{d}} = 5$ eV on Bi-5d.

Crystallographic Parameters													
Sample	a (Å)	b (Å)	c (Å)	$d_{\mathrm{Bi\text{-}O}}$ (Å)	$d_{\mathrm{Bi\text{-}I}}$ (Å)	B_0(GPa)	B_0'	α(°)	β(°)	γ(°)	V_0 (Å^3)	E_0 (eV)	R.F.
BiOI (Exp.)	3.9942(3)	3.9942(2)	9.1570(3)	2.338(×4)	3.371(×4)	–	–	90	90	90	146.0874(2)	–	χ^2=3.12
LDA	3.9777	3.9777	8.4351	2.324(×4)	3.298(×4)	80.9	4.03	90	90	90	133.4579	−31.271	–
GGA-PBE	4.0423	4.0423	9.2267	2.365(×4)	3.394(×4)	62.2	4.05	90	90	90	150.7664	−26.948	–
GGA-PBE+vdW	4.0169	4.0169	9.1267	2.331(×4)	3.064(×4)	83.8	4.06	90	90	90	147.2637	−28.453	–
GGA-PBEsol	4.0265	4.0265	9.1419	2.315(×4)	3.043(×4)	88.9	4.05	90	90	90	148.2149	−28.720	–
GGA-PBEsol+vdW	3.8610	3.8610	8.6588	2.306(×4)	3.017(×4)	97.6	4.04	90	90	90	105.9735	−30.761	–
DFT+U_{d}+U_{p}	4.0612	4.0612	10.1218	2.375(×4)	3.439(×4)	57.8	4.28	90	90	90	166.9443	−9.126	

VII. ELASTIC PROPERTIES

TABLE S4. Elastic constants (C_{ij}), bulk moduli (B_V, B_R and B_H), shear moduli (G_V, G_R, G_H), Young's moduli (E_V, E_R, E_H), Poisson's ratio (ν_V, ν_R, ν_H) and Pugh's ratio ($k_{Pugh,V}$, $k_{Pugh,R}$, $k_{Pugh,H}$) in Voigt–Reuss–Hill framework for BiOCl using LDA, GGA-PBE, GGA-PBE+vdW, GGA-PBEsol, GGA-PBEsol+vdW, and DFT+U_d+U_p XCFs. The λ_i are the eigenvalues of tensor C_{ij}.

Elastic Properties (E.P.) of BiOCl						
E.P.	LDA	PBE	PBE+vdW	PBEsol	PBEsol+vdW	DFT+U_d+U_p
C_{11} (GPa)	150.1	116.0	133.9	137.3	148.1	129.1
C_{12} (GPa)	80.4	53.7	69.4	70.8	80.7	48.5
C_{13} (GPa)	46.7	13.3	37.2	34.0	49.4	31.1
C_{33} (GPa)	72.3	9.9	53.7	43.5	82.5	33.1
C_{44} (GPa)	30.2	12.4	26.2	25.6	32.4	23.9
C_{66} (GPa)	68.3	50.4	60.4	62.0	69.2	51.2
B_V (GPa)	80.0	44.7	67.7	66.2	81.9	56.9
B_R (GPa)	65.4	9.8	50.4	42.3	71.4	32.9
B_H (GPa)	72.7	27.2	59.0	54.3	76.7	44.9
G_V (GPa)	39.0	25.8	34.4	34.6	40.1	31.8
G_R (GPa)	33.7	12.1	28.8	27.3	35.5	23.3
G_H (GPa)	36.3	18.9	31.6	30.9	37.8	27.6
E_V (GPa)	100.7	64.9	88.3	88.4	103.4	80.5
E_R (GPa)	86.2	25.6	72.6	67.4	91.3	56.5
E_H (GPa)	93.4	46.1	80.5	77.9	97.3	68.7
ν_V	0.290	0.260	0.280	0.280	0.290	0.260
ν_R	0.280	0.062	0.260	0.235	0.287	0.214
ν_H	0.286	0.218	0.273	0.261	0.288	0.246
$k_{Pugh,V}$	2.050	1.730	1.970	1.910	2.050	1.79
$k_{Pugh,R}$	1.941	0.809	1.749	1.554	2.012	1.417
$k_{Pugh,H}$	2.001	1.438	1.868	1.756	2.030	1.632
λ_1 (GPa)	30.2	7.7	26.2	25.6	32.4	20.7
λ_2 (GPa)	30.2	12.4	26.2	25.6	32.4	23.9
λ_3 (GPa)	48.3	12.4	37.0	30.5	54.5	23.9
λ_4 (GPa)	68.3	50.4	60.4	62.0	67.4	51.2
λ_5 (GPa)	69.7	62.3	64.5	66.6	69.2	80.7
λ_6 (GPa)	254.5	171.9	220.0	221.1	256.8	189.9

TABLE S5. Elastic constants (C_{ij}), bulk moduli (B_V, B_R and B_H), shear moduli (G_V, G_R, G_H), Young's moduli (E_V, E_R, E_H), Poisson's ratio (ν_V, ν_R, ν_H) and Pugh's ratio ($k_{Pugh,V}$, $k_{Pugh,R}$, $k_{Pugh,H}$) in Voigt–Reuss–Hill framework for BiOBr using LDA, GGA-PBE, GGA-PBE+vdW, GGA-PBEsol, GGA-PBEsol+vdW, and DFT+U_d+U_p XCFs. The λ_i are the eigenvalues of tensor C_{ij}.

Elastic Properties (E.P.) of of BiOBr						
E.P.	LDA	PBE	PBE+vdW	PBEsol	PBEsol+vdW	DFT+U_d+U_p
C_{11} (GPa)	132.1	94.9	117.3	115.9	134.8	96.4
C_{12} (GPa)	68.6	40.3	58.2	55.5	73.4	35.2
C_{13} (GPa)	31.1	4.3	23.6	16.9	37.9	4.3
C_{33} (GPa)	34.8	5.8	28.2	16.8	47.8	4.9
C_{44} (GPa)	25.8	3.2	20.9	15.4	32.9	3.5
C_{66} (GPa)	61.6	42.2	53.5	53.8	65.3	41.2
B_V (GPa)	62.3	32.6	52.6	47.5	68.4	31.7
B_R (GPa)	34.6	5.7	27.9	16.9	46.6	4.9
B_H (GPa)	48.4	19.2	40.3	32.2	57.5	18.3
G_V (GPa)	33.9	19.5	29.5	27.6	37.4	19.9
G_R (GPa)	25.1	5.2	21.7	16.5	29.9	5.3
G_H (GPa)	29.5	12.4	25.6	22.0	33.7	12.6
E_V (GPa)	85.9	48.8	74.6	69.3	94.9	49.4
E_R (GPa)	60.6	12.0	51.6	37.3	74.0	11.6
E_H (GPa)	73.5	30.5	63.4	53.8	84.6	30.7
ν_V	0.270	0.250	0.260	0.260	0.270	0.240
ν_R	0.208	0.150	0.191	0.132	0.235	0.101
ν_H	0.247	0.234	0.238	0.222	0.255	0.220
$k_{Pugh,V}$	1.840	1.670	1.780	1.720	1.830	1.590
$k_{Pugh,R}$	1.379	1.094	1.287	1.027	1.553	0.921
$k_{Pugh,H}$	1.644	1.550	1.572	1.463	1.707	1.452
λ_1 (GPa)	23.8	3.2	20.9	13.3	31.5	3.5
λ_2 (GPa)	25.8	3.2	20.9	15.4	32.9	3.5
λ_3 (GPa)	25.8	5.5	21.0	15.4	32.9	4.57
λ_4 (GPa)	61.6	42.2	53.5	53.8	61.4	41.2
λ_5 (GPa)	63.5	54.7	59.1	60.4	65.3	61.2
λ_6 (GPa)	211.6	135.6	182.7	174.9	224.4	131.8

TABLE S6. Elastic constants (C_{ij}), bulk moduli (B_V, B_R and B_H), shear moduli (G_V, G_R, G_H), Young's moduli (E_V, E_R, E_H), Poisson's ratio (ν_V, ν_R, ν_H) and Pugh's ratio ($k_{Pugh,V}$, $k_{Pugh,R}$, $k_{Pugh,H}$) in Voigt–Reuss–Hill framework for BiOI using LDA, GGA-PBE, GGA-PBE+vdW, GGA-PBEsol, GGA-PBEsol+vdW, and DFT+U_d+U_p XCFs. The λ_i are the eigenvalues of tensor C_{ij}.

Elastic Properties (E.P.) of BiOI						
E.P.	LDA	PBE	PBE+vdW	PBEsol	PBEsol+vdW	DFT+U_d+U_p
C_{11} (GPa)	124.0	96.1	184.2	191.8	207.1	86.1
C_{12} (GPa)	60.1	39.0	131.8	136.1	154.2	28.9
C_{13} (GPa)	35.6	14.3	91.1	93.63	109.9	3.8
C_{33} (GPa)	47.4	25.2	130.9	124.9	178.5	4.6
C_{44} (GPa)	28.8	10.6	78.64	78.9	92.4	7.7
C_{66} (GPa)	54.8	39.9	122.4	126.8	143.7	34.8
B_V (GPa)	62.0	39.2	125.3	128.4	148.9	27.8
B_R (GPa)	45.4	23.4	116.1	115.3	144.7	4.6
B_H (GPa)	53.7	31.3	120.7	121.8	146.9	16.2
G_V (GPa)	33.4	22.2	68.3	69.3	80.3	19.4
G_R (GPa)	27.9	15.3	48.9	49.0	56.4	7.6
G_H (GPa)	30.7	18.7	58.6	59.2	68.4	13.5
E_V (GPa)	85.0	56.0	173.4	176.2	204.2	47.2
E_R (GPa)	69.5	37.6	128.8	128.8	149.8	14.8
E_H (GPa)	77.3	46.9	151.4	152.7	177.5	31.7
ν_V	0.270	0.260	0.270	0.270	0.270	0.22
ν_R	0.245	0.231	0.315	0.314	0.327	−0.031
ν_H	0.260	0.250	0.291	0.291	0.299	0.175
$k_{Pugh,V}$	1.860	1.770	1.830	1.850	1.860	1.440
$k_{Pugh,R}$	1.625	1.529	2.369	2.351	2.564	0.608
$k_{Pugh,H}$	1.750	1.670	2.057	2.059	2.148	1.203
λ_1 (GPa)	28.8	10.6	52.4	55.8	52.9	4.4
λ_2 (GPa)	28.8	10.6	64.8	59.6	89.6	7.7
λ_3 (GPa)	30.8	21.6	78.6	78.9	92.4	7.7
λ_4 (GPa)	54.8	39.9	78.6	78.9	92.4	34.8
λ_5 (GPa)	122.4	57.1	122.4	126.8	143.7	57.2
λ_6 (GPa)	200.7	138.8	382.1	393.3	450.2	115.4

VIII. RAMAN ANALYSIS

TABLE S7. Experimental (Exp.) room temperature Raman peaks of BiOCl compared against those obtained from DFT simulations using LDA, GGA-PBE, and GGA-PBEsol XCFs. ISSM: Internal Symmetric Stretching Mode, AVM: Antisymmetric Vibration Mode, and SSM: Symmetric Stretching Mode.

Raman Peak Analysis of BiOCl					
Exp. (cm^{-1})	LDA (cm^{-1})	GGA-PBE (cm^{-1})	GGA-PBEsol (cm^{-1})	Symm.	Peak Assignment
123(2)	136	118	131	A_{1g}	Bi-Cl ISSM
147(2)	151	143	144	A_{1g}	Bi-Cl ISSM
198(2)	207	202	198	E_g	Bi-Cl ISSM
300(2)	288	272	280	B_{1g}	Bi-O AVM
496(2)	509	494	408	E_g	Bi-O SSM
527(2)	528	512	511	E_g	Bi-O SSM

TABLE S8. Experimental room temperature Raman peaks of BiOBr compared against those obtained from DFT simulations using LDA, GGA-PBE, and GGA-PBEsol XCFs. ISSM: Internal Symmetric Stretching Mode, AVM: Antisymmetric Vibration Mode, and SSM: Symmetric Stretching Mode.

Raman Peak Analysis of BiOBr					
Exp. (cm^{-1})	LDA (cm^{-1})	GGA-PBE (cm^{-1})	GGA-PBEsol (cm^{-1})	Symm.	Peak Assignment
112(2)	105	100	104	A_{1g}	Bi-Br ISSM
116(2)	114	113	114	A_{1g}	Bi-Br ISSM
162(2)	150	147	149	E_g	Bi-Br ISSM
181(2)	183	187	184	E_g	Bi-Br ISSM
385(2)	387	391	387	B_{1g}	Bi-O AVM

TABLE S9. Experimental (Exp.) room temperature Raman peaks of BiOI compared against those obtained from DFT simulations using LDA, GGA-PBE, and GGA-PBEsol XCFs. ISSM: Internal Symmetric Stretching Mode, AVM: Antisymmetric Vibration Mode, and SSM: Symmetric Stretching Mode.

Raman Peak Analysis of BiOI					
Exp. (cm^{-1})	LDA (cm^{-1})	GGA-PBE (cm^{-1})	GGA-PBEsol (cm^{-1})	Symm.	Peak Assignment
67(2)	72	70	77	A_{1g}	Bi-I ISSM
85(2)	83	79	89	A_{1g}	Bi-I ISSM
98(2)	96	99	100	A_{1g}	Bi-I ISSM
148(2)	115	–	142	E_g	Bi-I ISSM
591(2)	451	418	472	B_{1g}	Bi-O AVM
1019(2)	–	–	–	A_{1g}	Bi-O SVM

IX. FTIR ANALYSIS

TABLE S10. Experimental (Exp.) room temperature FTIR peaks of BiOCl compared against those obtained from phonon DOS simulations using LDA, GGA-PBE, GGA-PBE+vdW, GGA-PBEsol, GGA-PBEsol+vdW, and DFT+U_{d}+U_{p} XCFs. SVM: Stretching Vibration Mode and BVM: Bending Vibration Mode.

FTIR Peak Analysis of BiOCl							
Exp. (cm^{-1})	LDA (cm^{-1})	PBE (cm^{-1})	PBE+vdW (cm^{-1})	PBEsol (cm^{-1})	PBEsol+vdW (cm^{-1})	DFT+U_{d}+U_{p} (cm^{-1})	Peak Assign.
355(4)	–	332	337	351	–		Bi-O SVM
366(4)	363	–	–	–	362	361	Bi-O SVM
385(4)	413	383	–	–	–	381	Bi-O SVM
530(4)	500	–	476	487	500		Bi-O SVM
650(4)	–	–	–	–	–		Bi-O SVM
718(4)	–	–	–	–	–		Bi-O SVM
926(4)	–	–	–	–	–		Bi-O SVM
1016(4)	–	–	–	–	–		Bi-Cl SVM
1305(4)	–	–	–	–	–		Bi-Cl SVM
1332(4)	–	–	–	–	–		Bi-Cl SVM
1396(4)	–	–	–	–	–		Bi-Cl SVM
1534(4)	–	–	–	–	–		Bi-Cl SVM
1620(4)	–	–	–	–	–		O-H BVM
1720(4)	–	–	–	–	–		C=O SVM
3544(4)	–	–	–	–	–		O-H SVM

TABLE S11. Experimental (Exp.) room temperature FTIR peaks of BiOBr compared against those obtained from phonon DOS simulations using LDA, GGA-PBE, GGA-PBE+vdW, GGA-PBEsol, GGA-PBEsol+vdW, and DFT+U_{d}+U_{p} XCFs.

FTIR Peak Analysis of BiOBr							
Exp. (cm^{-1})	LDA (cm^{-1})	PBE (cm^{-1})	PBE+vdW (cm^{-1})	PBEsol (cm^{-1})	PBEsol+vdW (cm^{-1})	DFT+U_{d}+U_{p} (cm^{-1})	Peak Assign.
372(4)	354	377	376	385	–	368	Bi-O SVM
405(4)	396	415	401	418	390	410	Bi-O SVM
440(4)	441	442	439	441	433	440	Bi-O SVM
505(4)	481	460	462	473	480		Bi-O SVM
760(4)	–	–	–	–	–		Bi-O SVM
870(4)	–	–	–	–	–		Bi-O SVM
1090(4)	–	–	–	–	–		Bi-Cl SVM
1280(4)	–	–	–	–	–		Bi-Cl SVM
1451(4)	–	–	–	–	–		Bi-Cl SVM
1620(4)	–	–	–	–	–		O-H BVM
1720(4)	–	–	–	–	–		C=O SVM
3430(4)	–	–	–	–	–		O-H SVM

TABLE S12. Experimental (Exp.) room temperature FTIR peaks of BiOI compared against those obtained from phonon DOS simulations using LDA, GGA-PBE, GGA-PBE+vdW, GGA-PBEsol, GGA-PBEsol+vdW, and DFT+U_{d}+U_{p} XCFs.

FTIR Peak Analysis of BiOI							
Exp. (cm^{-1})	LDA (cm^{-1})	PBE (cm^{-1})	PBE+vdW (cm^{-1})	PBEsol (cm^{-1})	PBEsol+vdW (cm^{-1})	DFT+U_{d}+U_{p} (cm^{-1})	Peak Assign.
365(4)	372	367	–	362	372	360	Bi-O SVM
392(4)	400	398	–	392	395	391	Bi-O SVM
407(4)	412	405	–	405	414	408	Bi-O SVM
428(4)	431	422	–	418	421	420	Bi-O SVM
472(4)	454	–	–	470	467		Bi-O SVM
612(4)	–	–	–	–	–		Bi-O SVM
750(4)	–	–	–	–	–		Bi-O SVM
815(4)	–	–	–	–	–		Bi-O SVM
950(4)	–	–	–	–	–		Bi-O SVM
1105(4)	–	–	–	–	–		Bi-Cl SVM
1312(4)	–	–	–	–	–		Bi-Cl SVM
1382(4)	–	–	–	–	–		Bi-Cl SVM
1615(4)	–	–	–	–	–		O-H BVM
3427(4)	–	–	–	–	–		O-H SVM

X. PHONON VIBRATIONAL SPECTROSCOPY

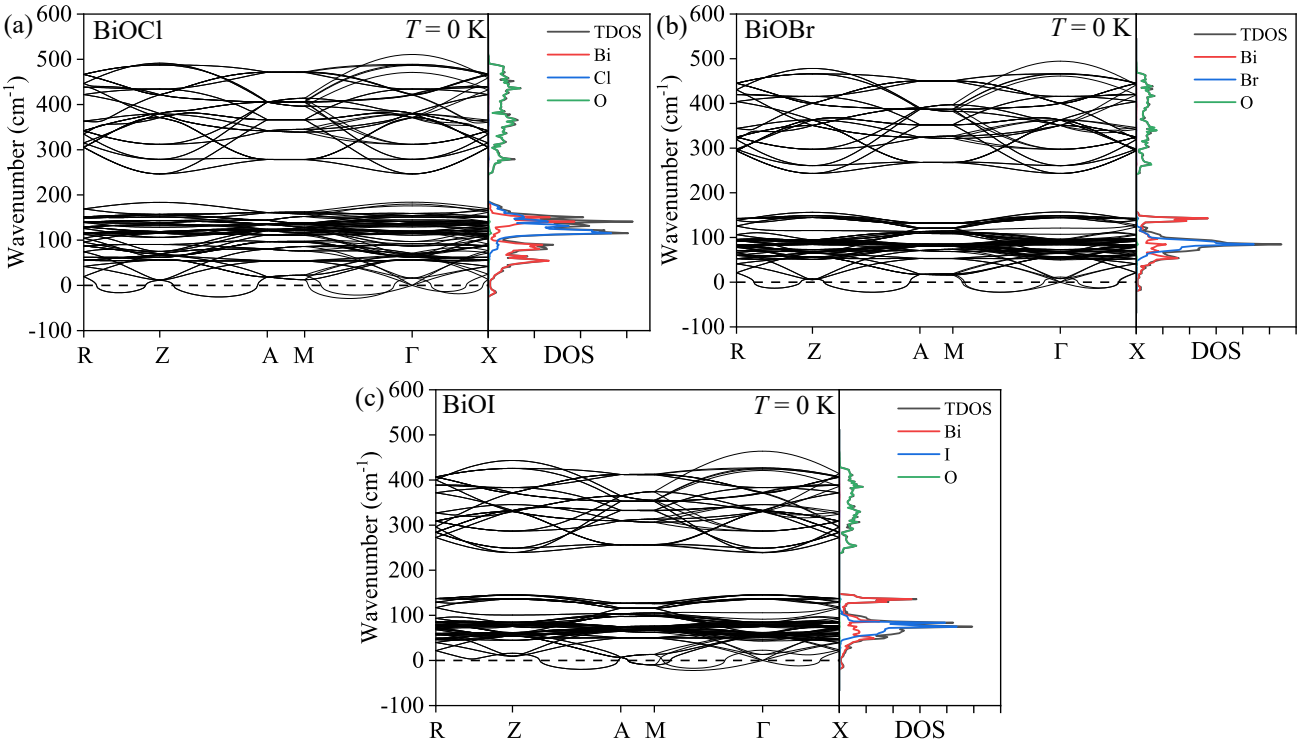

FIG. S4. Phonon BS and DOS of Bi, O, and Cl atoms in BiOCl using DFPT at GGA-PBE level. The phonon BS is simulated along A, Γ, M, R, X, and Z high symmetry k-points in BZ.

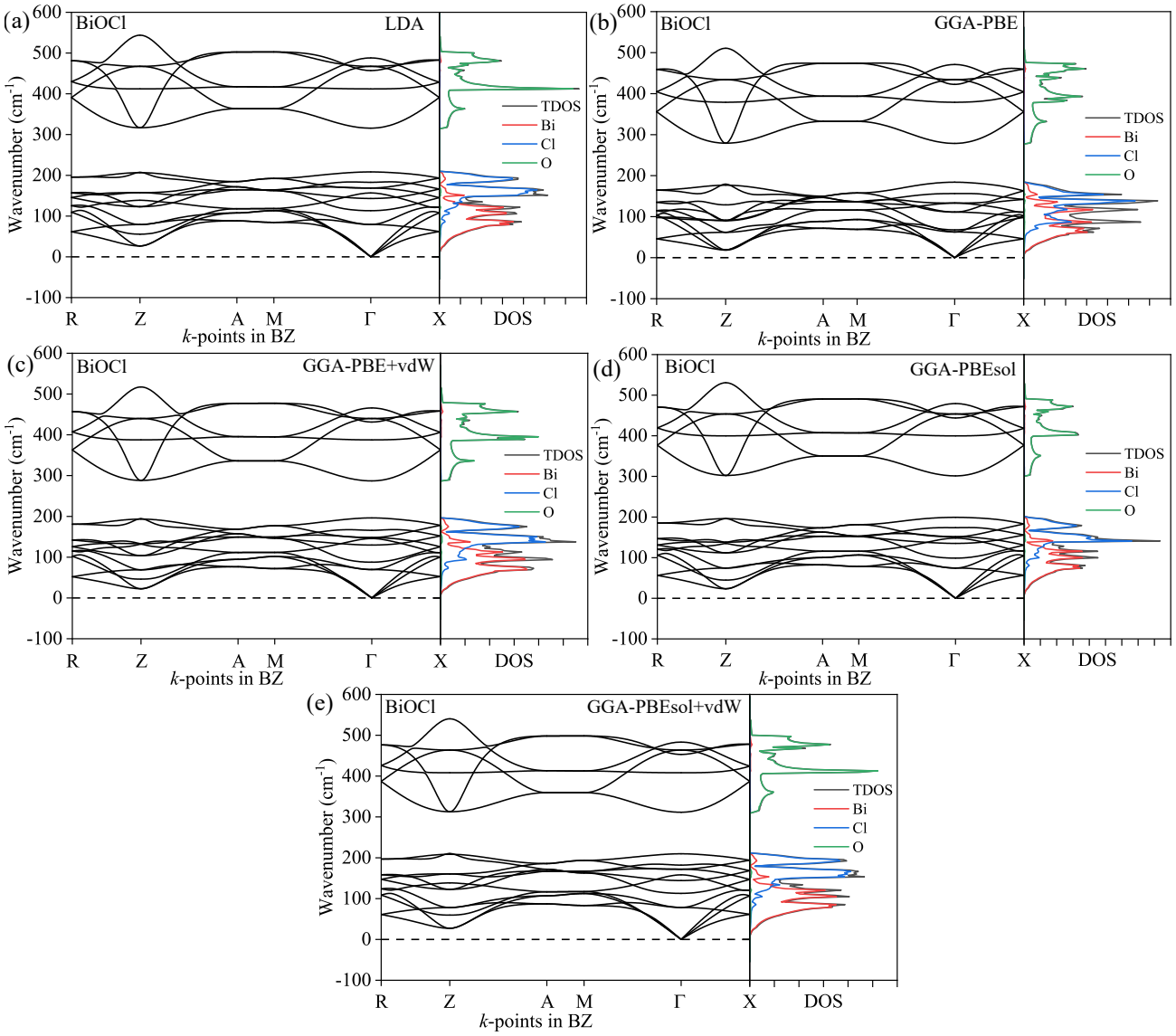

FIG. S5. Phonon BS, total DOS, and partial DOS of Bi, O, and Cl atoms in BiOCl using $4 \times 4 \times 4$ supercell based finite difference technique for (a) LDA, (b) GGA-PBE, (c) GGA-PBE+vdW, (d) GGA-PBEsol, and (e) GGA-PBEsol+vdW. The phonon BS is simulated along A, Γ, M, R, X, and Z high symmetry k-points in BZ.

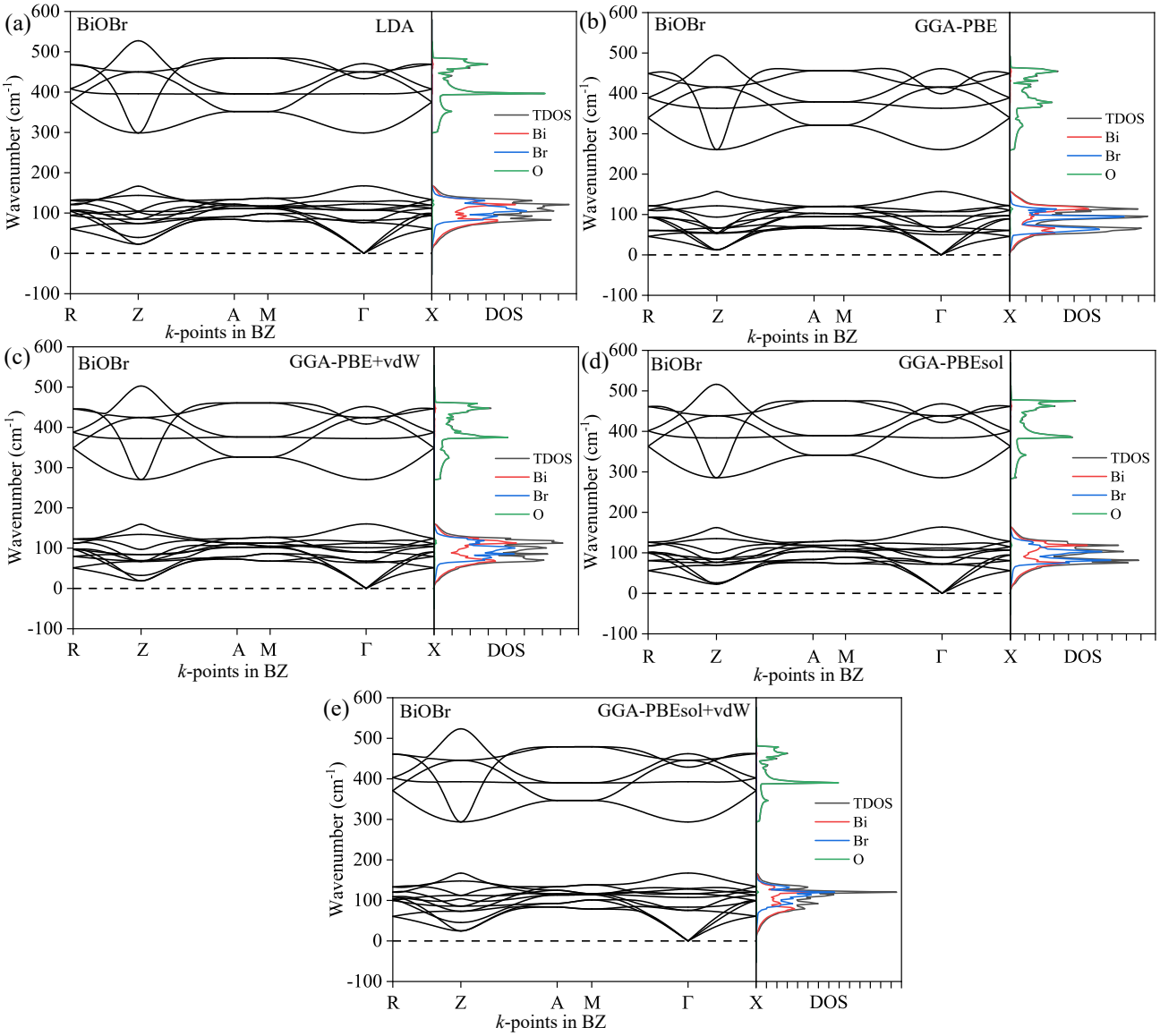

FIG. S6. Phonon BS, total DOS, and partial DOS of Bi, O, and Br atoms in BiOBr using $4 \times 4 \times 4$ supercell based finite difference technique for (a) LDA, (b) GGA-PBE, (c) GGA-PBE+vdW, (d) GGA-PBEsol, and (e) GGA-PBEsol+vdW. The phonon BS is simulated along A, Γ, M, R, X, and Z high symmetry k-points in BZ.

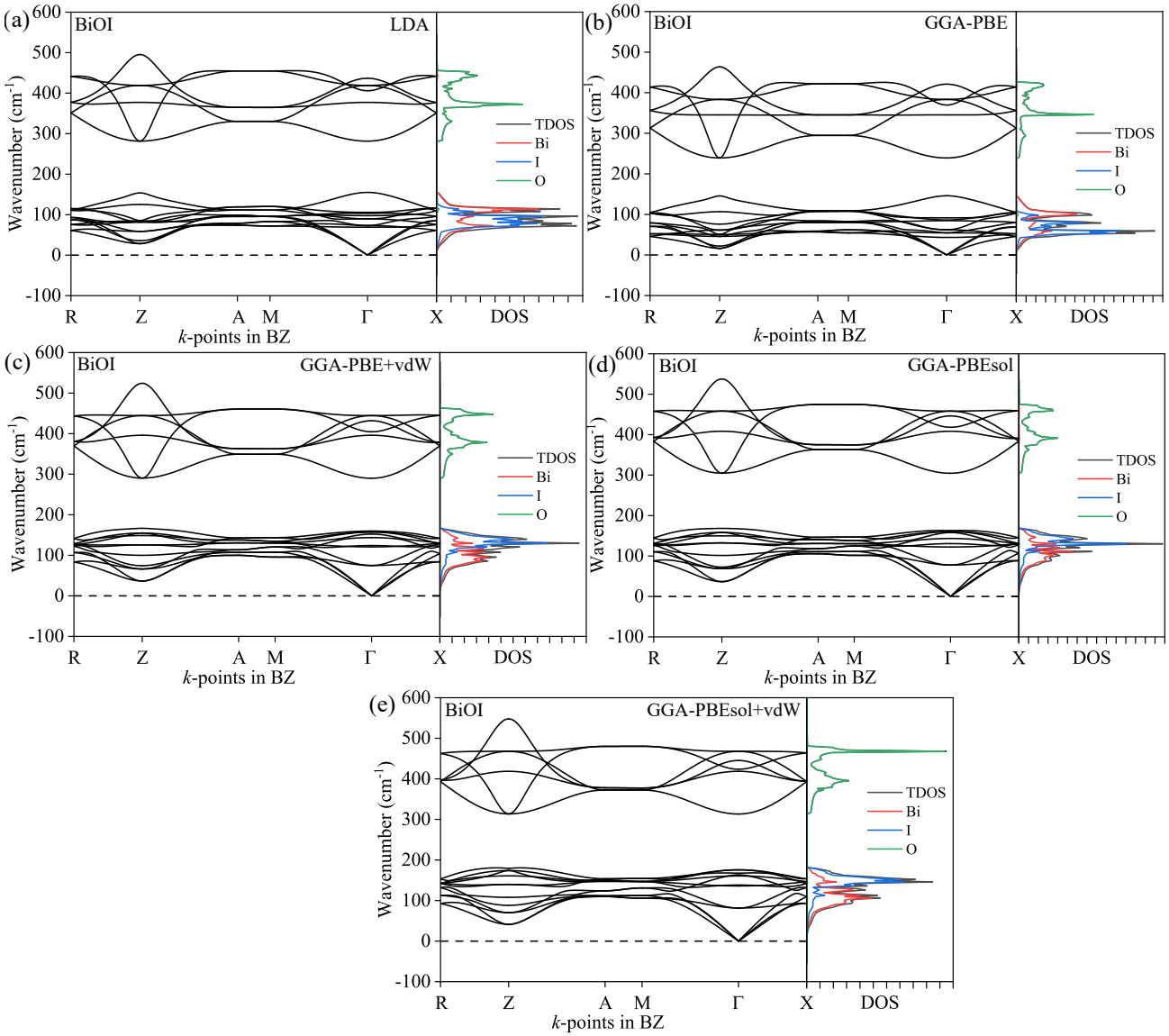

FIG. S7. Phonon BS, total DOS, and partial DOS of Bi, O, and I atoms in BiOI using $4 \times 4 \times 4$ supercell based finite difference technique for (a) LDA, (b) GGA-PBE, (c) GGA-PBE+vdW, (d) GGA-PBEsol, and (e) GGA-PBEsol+vdW. The phonon BS is simulated along A, Γ, M, R, X, and Z high symmetry k-points in BZ.

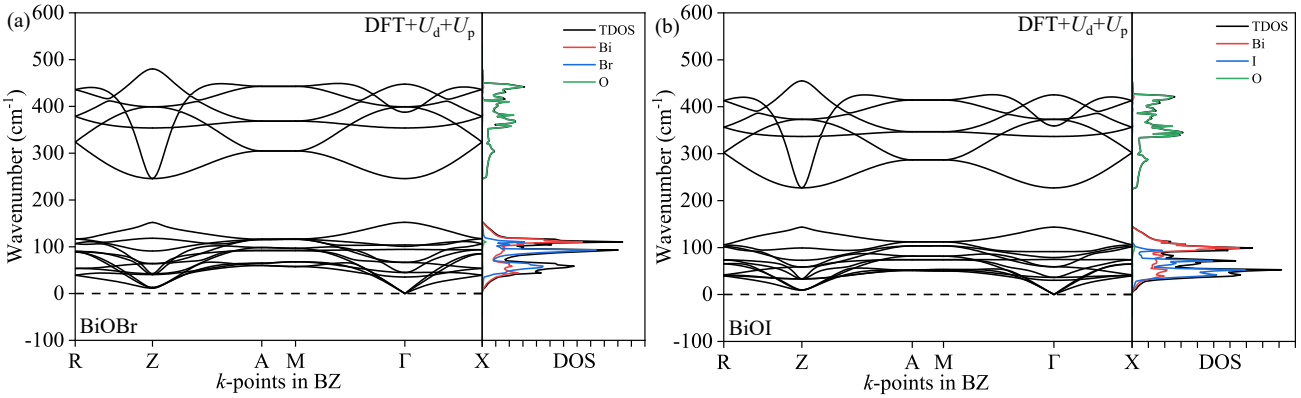

FIG. S8. Phonon BS along A, M, Γ, R, X, and Z and DOS of (a) BiOBr, and (b) BiOI with $4 \times 4 \times 4$ supercell based finite difference technique at DFT+U_d+U_p level.

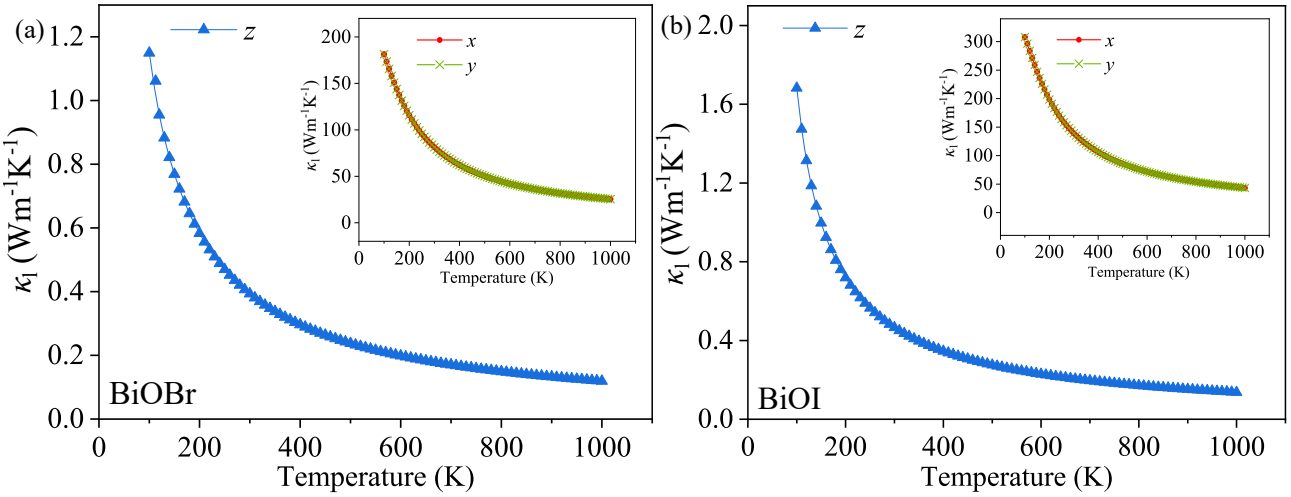

FIG. S9. Temperature-dependent lattice thermal conductivity κ_l of (a) BiOBr, and (b) BiOI with $4 \times 4 \times 4$ supercell based finite difference technique at DFT+U_d+U_p level.

XI. BORN CHARGE

The Born effective charge (BEC) embodies the atomic charge dynamics. The BEC has its origin in the screening of long-range Coulomb potential of the ions whose motion forms the phonon characteristics. The simulated BEC tensors were displayed in Table S13, Table S14, and Table S15.

TABLE S13. Born effective charge tensor of BiOCl using $4 \times 4 \times 4$ supercell based finite difference technique with LDA, GGA-PBE, GGA-PBE+vdW, GGA-PBEsol, GGA-PBEsol+vdW, and DFT+U_{d}+U_{p} XCFs with NAC on.

XCF	Z_B	Position	xx	xy	xz	yx	yy	yz	zx	zy	zz
LDA	Bi	2c	5.355	0.000	0.000	0.000	5.355	0.000	0.000	0.000	3.775
	O	2a	−3.270	0.000	0.000	0.000	−3.270	0.000	0.000	0.000	−2.246
	Cl	2c	−2.085	0.000	0.000	0.000	−2.085	0.000	0.000	0.000	−1.529
GGA-PBE	Bi	2c	6.230	0.000	0.000	0.000	6.230	0.000	0.000	0.000	4.241
	O	2a	−3.266	0.000	0.000	0.000	−3.266	0.000	0.000	0.000	−1.728
	Cl	2c	−2.119	0.000	0.000	0.000	−2.119	0.000	0.000	0.000	−1.136
GGA-PBE+vdW	Bi	2c	5.352	0.000	0.000	0.000	5.352	0.000	0.000	0.000	3.632
	O	2a	−3.261	0.000	0.000	0.000	−3.261	0.000	0.000	0.000	−2.129
	Cl	2c	−2.091	0.000	0.000	0.000	−2.091	0.000	0.000	0.000	−1.503
GGA-PBEsol	Bi	2c	5.370	0.000	0.000	0.000	5.370	0.000	0.000	0.000	3.549
	O	2a	−3.270	0.000	0.000	0.000	−3.270	0.000	0.000	0.000	−2.111
	Cl	2c	−2.100	0.000	0.000	0.000	−2.100	0.000	0.000	0.000	−1.439
GGA-PBEsol+vdW	Bi	2c	5.338	0.000	0.000	0.000	5.338	0.000	0.000	0.000	3.868
	O	2a	−3.258	0.000	0.000	0.000	−3.258	0.000	0.000	0.000	−2.289
	Cl	2c	−2.080	0.000	0.000	0.000	−2.080	0.000	0.000	0.000	−1.579
DFT+U_{d}+U_{p}	Bi	2c	5.400	0.000	0.000	0.000	5.400	0.000	0.000	0.000	3.501
	O	2a	−3.319	0.000	0.000	0.000	−3.319	0.000	0.000	0.000	−1.955
	Cl	2c	−2.081	0.000	0.000	0.000	−2.081	0.000	0.000	0.000	−1.546

TABLE S14. Born effective charge tensor of BiOBr using $4 \times 4 \times 4$ supercell based finite difference technique with LDA, GGA-PBE, GGA-PBE+vdW, GGA-PBEsol, GGA-PBEsol+vdW, and DFT+U_{d}+U_{p} XCFs with NAC on.

XCF	Z_B	Position	xx	xy	xz	yx	yy	yz	zx	zy	zz
LDA	Bi	2c	5.658	0.000	0.000	0.000	5.658	0.000	0.000	0.000	3.623
	O	2a	−3.509	0.000	0.000	0.000	−3.509	0.000	0.000	0.000	−2.367
	Br	2c	−2.149	0.000	0.000	0.000	−2.149	0.000	0.000	0.000	−1.256
GGA-PBE	Bi	2c	5.589	0.000	0.000	0.000	5.589	0.000	0.000	0.000	2.439
	O	2a	−3.463	0.000	0.000	0.000	−3.463	0.000	0.000	0.000	−1.612
	Br	2c	−2.126	0.000	0.000	0.000	−2.126	0.000	0.000	0.000	−0.826
GGA-PBE+vdW	Bi	2c	5.637	0.000	0.000	0.000	5.637	0.000	0.000	0.000	3.396
	O	2a	−3.484	0.000	0.000	0.000	−3.484	0.000	0.000	0.000	−2.195
	Br	2c	−2.153	0.000	0.000	0.000	−2.153	0.000	0.000	0.000	−1.200
GGA-PBEsol	Bi	2c	5.630	0.000	0.000	0.000	5.630	0.000	0.000	0.000	3.195
	O	2a	−3.487	0.000	0.000	0.000	−3.487	0.000	0.000	0.000	−2.097
	Br	2c	−2.143	0.000	0.000	0.000	−2.143	0.000	0.000	0.000	−1.098
GGA-PBEsol+vdW	Bi	2c	5.665	0.000	0.000	0.000	5.665	0.000	0.000	0.000	3.867
	O	2a	−3.504	0.000	0.000	0.000	−3.504	0.000	0.000	0.000	−2.506
	Br	2c	−2.160	0.000	0.000	0.000	−2.160	0.000	0.000	0.000	−1.361
DFT+U_{d}+U_{p}	Bi	2c	5.624	0.000	0.000	0.000	5.624	0.000	0.000	0.000	2.405
	O	2a	−3.4864	0.000	0.000	0.000	−3.486	0.000	0.000	0.000	−1.589
	Br	2c	−2.138	0.000	0.000	0.000	−2.138	0.000	0.000	0.000	−0.817

TABLE S15. Born effective charge tensor of BiOI using $4 \times 4 \times 4$ supercell based finite difference technique with LDA, GGA-PBE, GGA-PBE+vdW, GGA-PBEsol, GGA-PBEsol+vdW, and DFT+U_{d}+U_{p} XCFs with NAC on.

XCF	Z_B	Position	xx	xy	xz	yx	yy	yz	zx	zy	zz
LDA	Bi	2c	6.132	0.000	0.000	0.000	6.132	0.000	0.000	0.000	3.924
	O	2a	−3.949	0.000	0.000	0.000	−3.949	0.000	0.000	0.000	−2.773
	I	2c	−2.183	0.000	0.000	0.000	−2.183	0.000	0.000	0.000	−1.151
GGA-PBE	Bi	2c	6.007	0.000	0.000	0.000	6.007	0.000	0.000	0.000	3.172
	O	2a	−3.844	0.000	0.000	0.000	−3.844	0.000	0.000	0.000	−2.202
	I	2c	−2.162	0.000	0.000	0.000	−2.162	0.000	0.000	0.000	−0.970
GGA-PBE+vdW	Bi	2c	6.369	0.000	0.000	0.000	6.369	0.000	0.000	0.000	4.917
	O	2a	−3.904	0.000	0.000	0.000	−3.904	0.000	0.000	0.000	−3.733
	I	2c	−2.466	0.000	0.000	0.000	−2.466	0.000	0.000	0.000	−1.184
GGA-PBEsol	Bi	2c	6.392	0.000	0.000	0.000	6.392	0.000	0.000	0.000	4.811
	O	2a	−3.934	0.000	0.000	0.000	−3.934	0.000	0.000	0.000	−3.700
	I	2c	−2.458	0.000	0.000	0.000	−2.458	0.000	0.000	0.000	−1.111
GGA-PBEsol+vdW	Bi	2c	6.377	0.000	0.000	0.000	6.377	0.000	0.000	0.000	5.214
	O	2a	−3.936	0.000	0.000	0.000	−3.936	0.000	0.000	0.000	−4.022
	I	2c	−2.441	0.000	0.000	0.000	−2.441	0.000	0.000	0.000	−1.191
DFT+U_{d}+U_{p}	Bi	2c	5.944	0.000	0.000	0.000	5.944	0.000	0.000	0.000	2.437
	O	2a	−3.812	0.000	0.000	0.000	−3.812	0.000	0.000	0.000	−1.686
	I	2c	−2.131	0.000	0.000	0.000	−2.131	0.000	0.000	0.000	−0.751

XII. EDX ANALYSIS

TABLE S16. Bi, O, Cl, Br and I element identification, atomic percentage at. (%) and weight percentage wt. (%) concentration analysis of BiOCl, BiOBr, and BiOI using EDX (Model: EDAX Team).

EDX Analysis of BiOCl, BiOBr, and BiOI					
Sample	Element	at. (%) (Theory)	at. (%) (Exp.)	wt. (%) (Theory)	wt. (%) (Exp.)
BiOCl	Bi	33.33	29.90	80.25	79.74
	O	33.33	45.50	6.14	9.63
	Cl	33.34	24.60	13.61	10.63
BiOBr	Bi	33.33	30.70	68.54	68.07
	O	33.33	39.50	5.25	7.75
	Br	33.34	29.80	26.21	25.18
BiOI	Bi	33.33	37.79	59.39	59.25
	O	33.33	27.08	4.55	3.44
	I	33.34	37.13	36.06	37.31

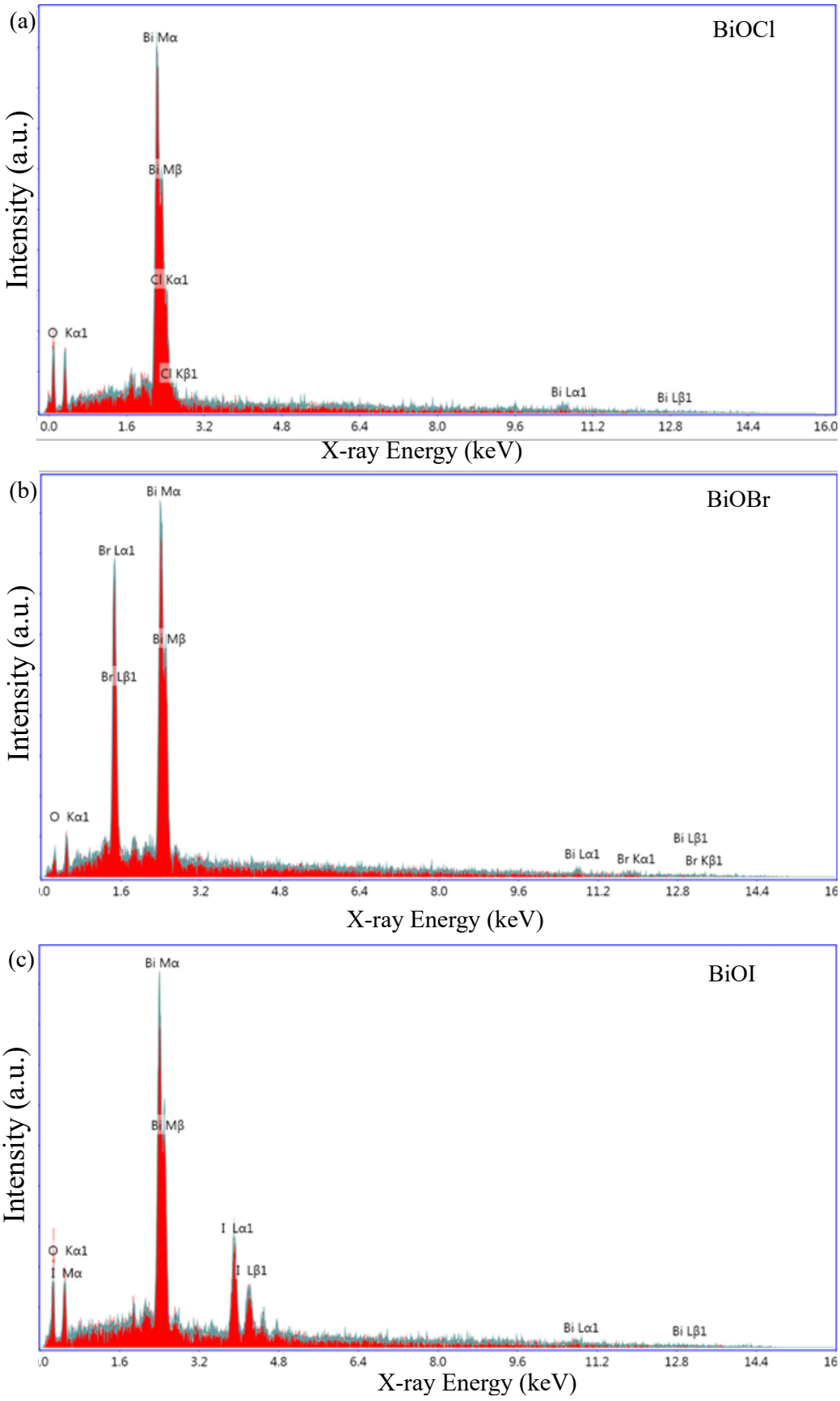

FIG. S10. EDX spectra of (a) BiOCl, (b) BiOBr, and (c) BiOI.

XIII. OPTICAL PROPERTIES

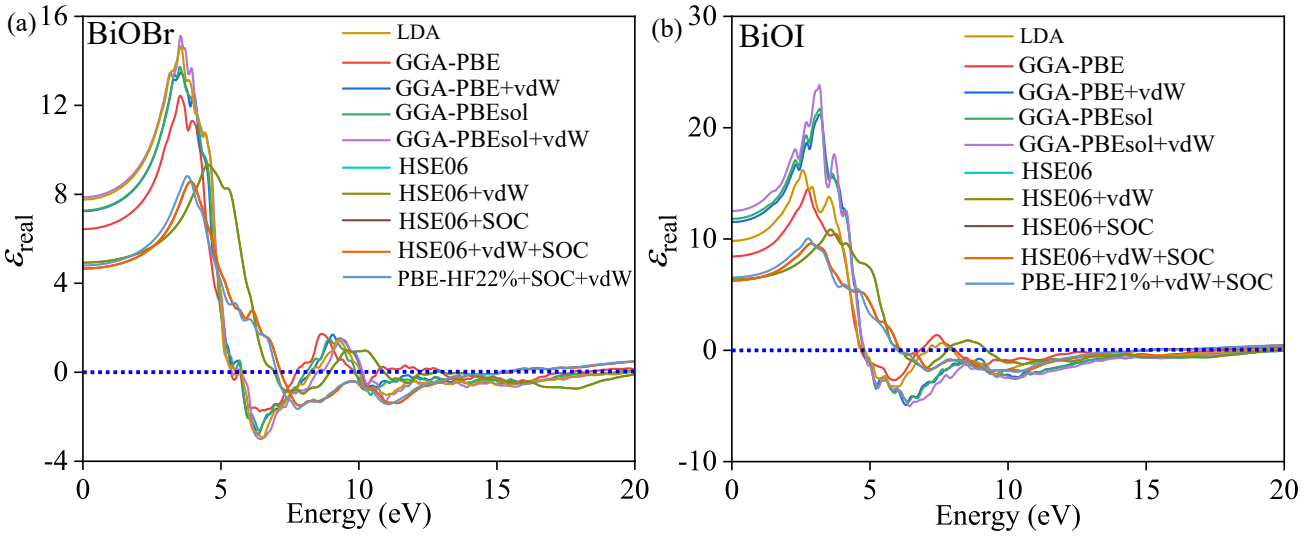

FIG. S11. Real part of the dielectric constant $\varepsilon_{\text{real}}$ of (a) BiOBr, and (b) BiOI as a function of photon energy for different XCFs.

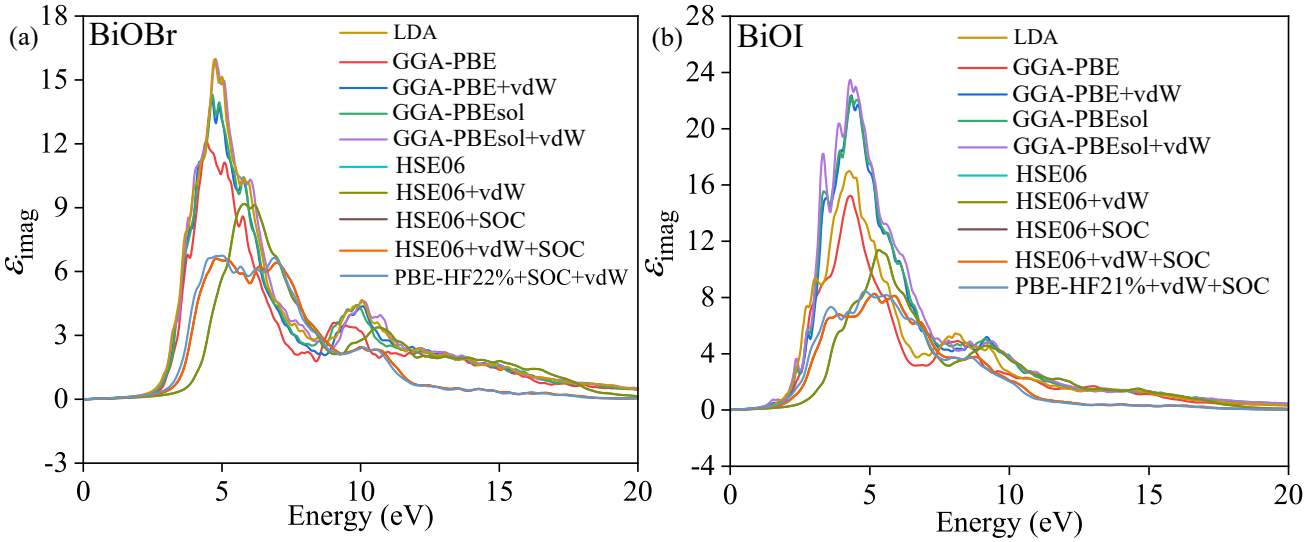

FIG. S12. Imaginary part of the dielectric constant $\varepsilon_{\text{imag}}$ of (a) BiOBr, and (b) BiOI as a function of photon energy for different XCFs.

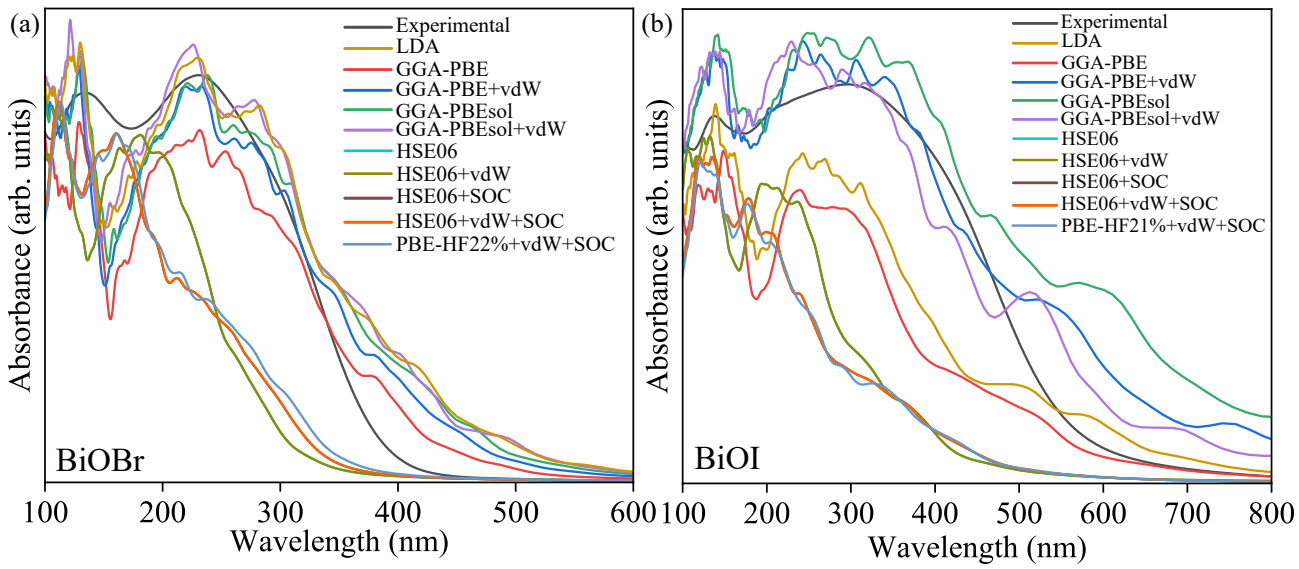

FIG. S13. Experimental and simulated optical absorption for (a) BiOBr, and (b) BiOI for different XCFs.

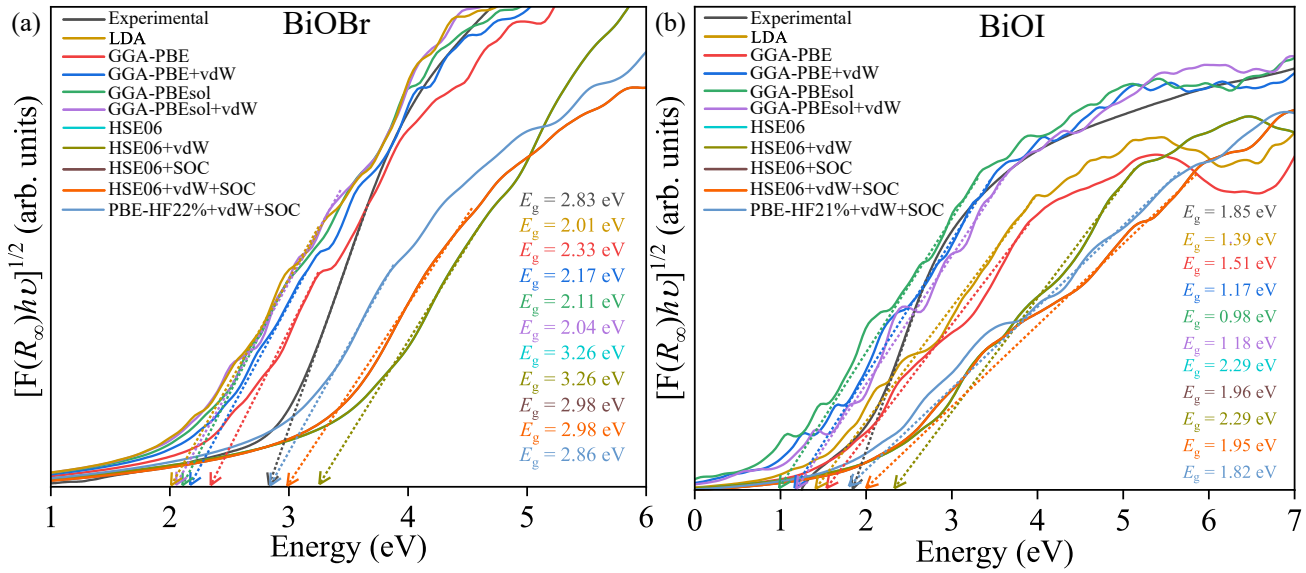

FIG. S14. Experimental and simulated Tauc plots for (a) BiOBr, and (b) BiOI for different XCFs.

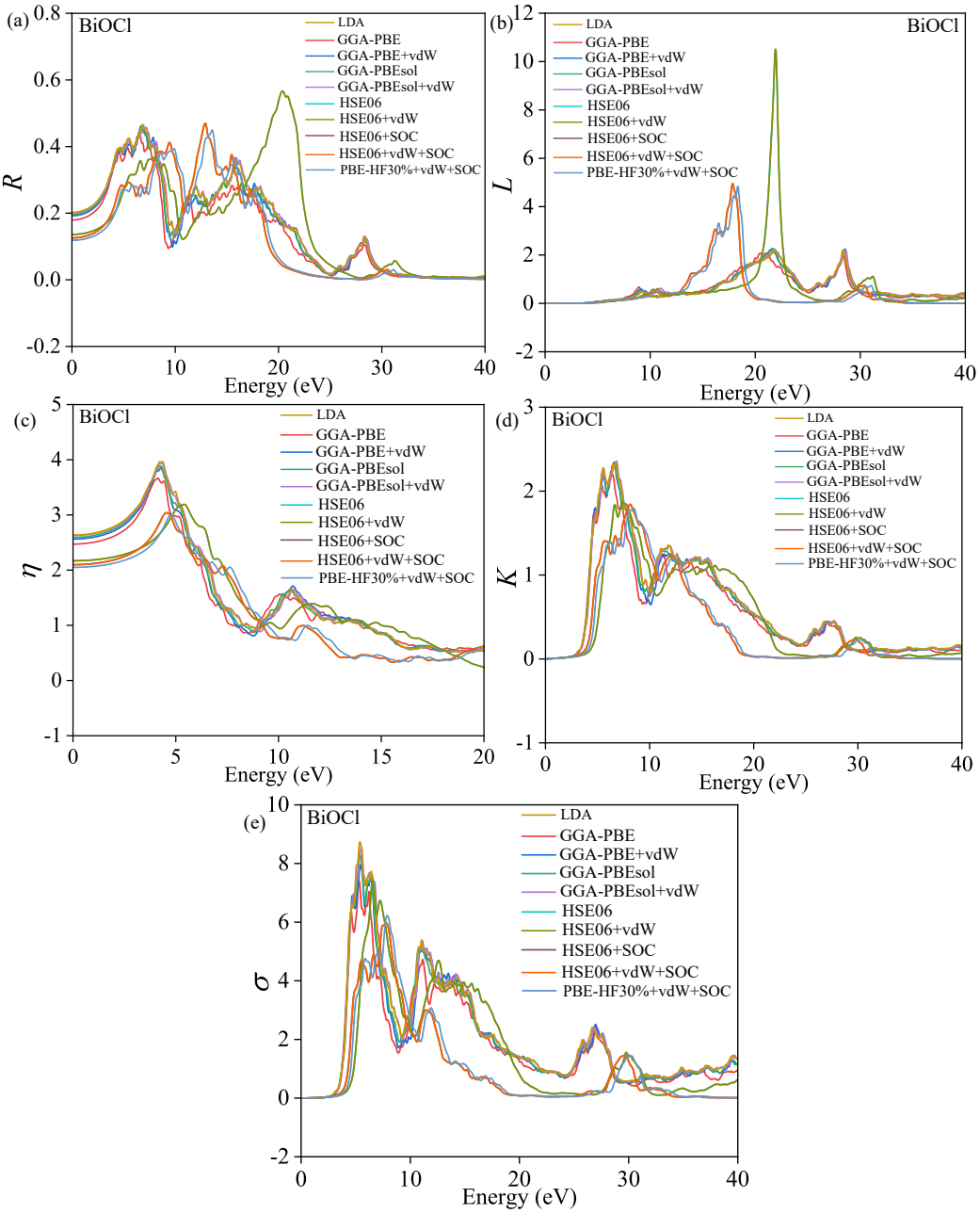

FIG. S15. Linear optical properties: (a) reflectance (R), (b) loss function (L), (c) refractive index (η), (d) extinction coefficient (K), and (e) optical conductivity (σ) of BiOCl for different XCFs.

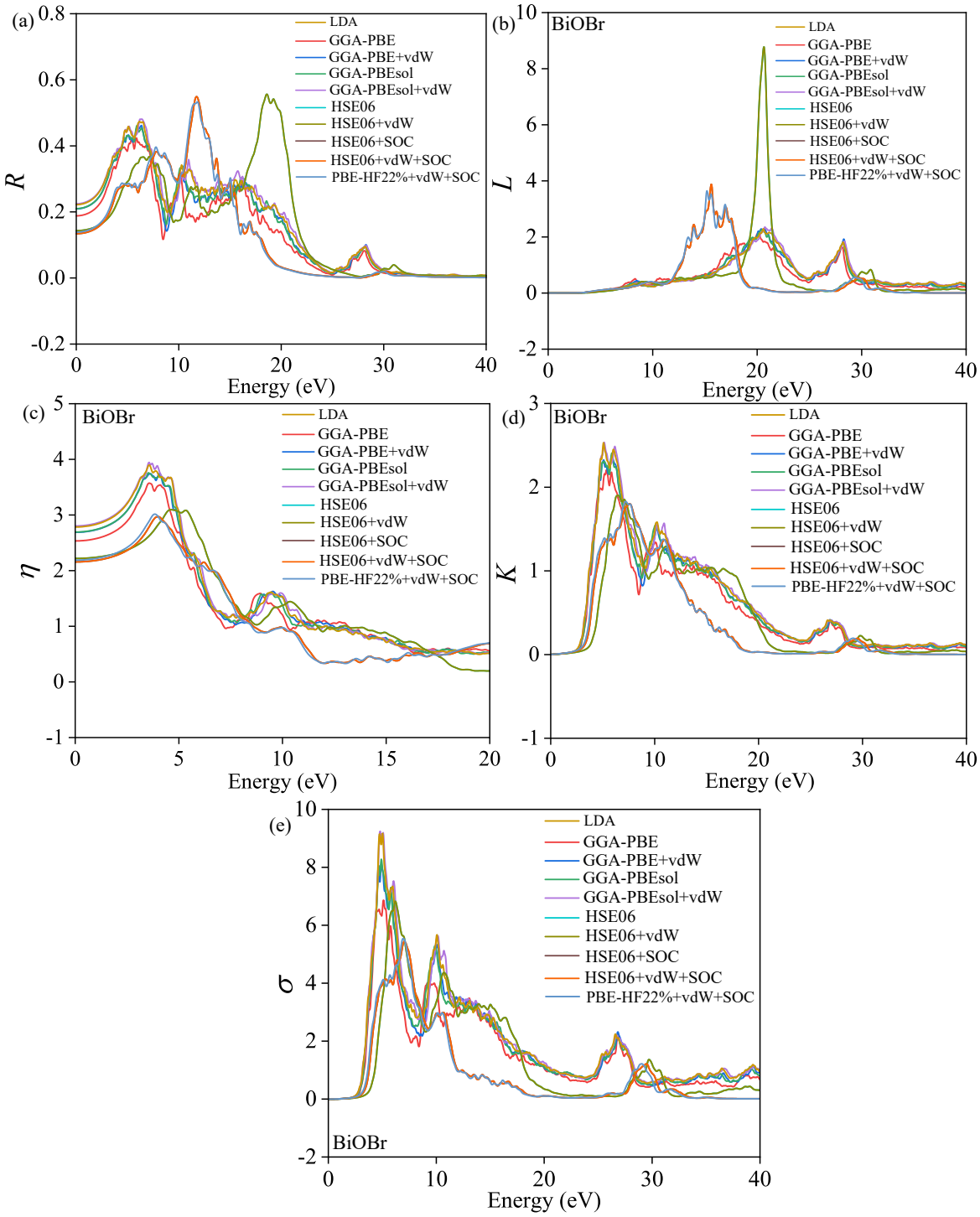

FIG. S16. Linear optical properties: (a) reflectance (R), (b) loss function (L), (c) refractive index (η), (d) extinction coefficient (K), and (e) optical conductivity (σ) of BiOBr for different XCFs.

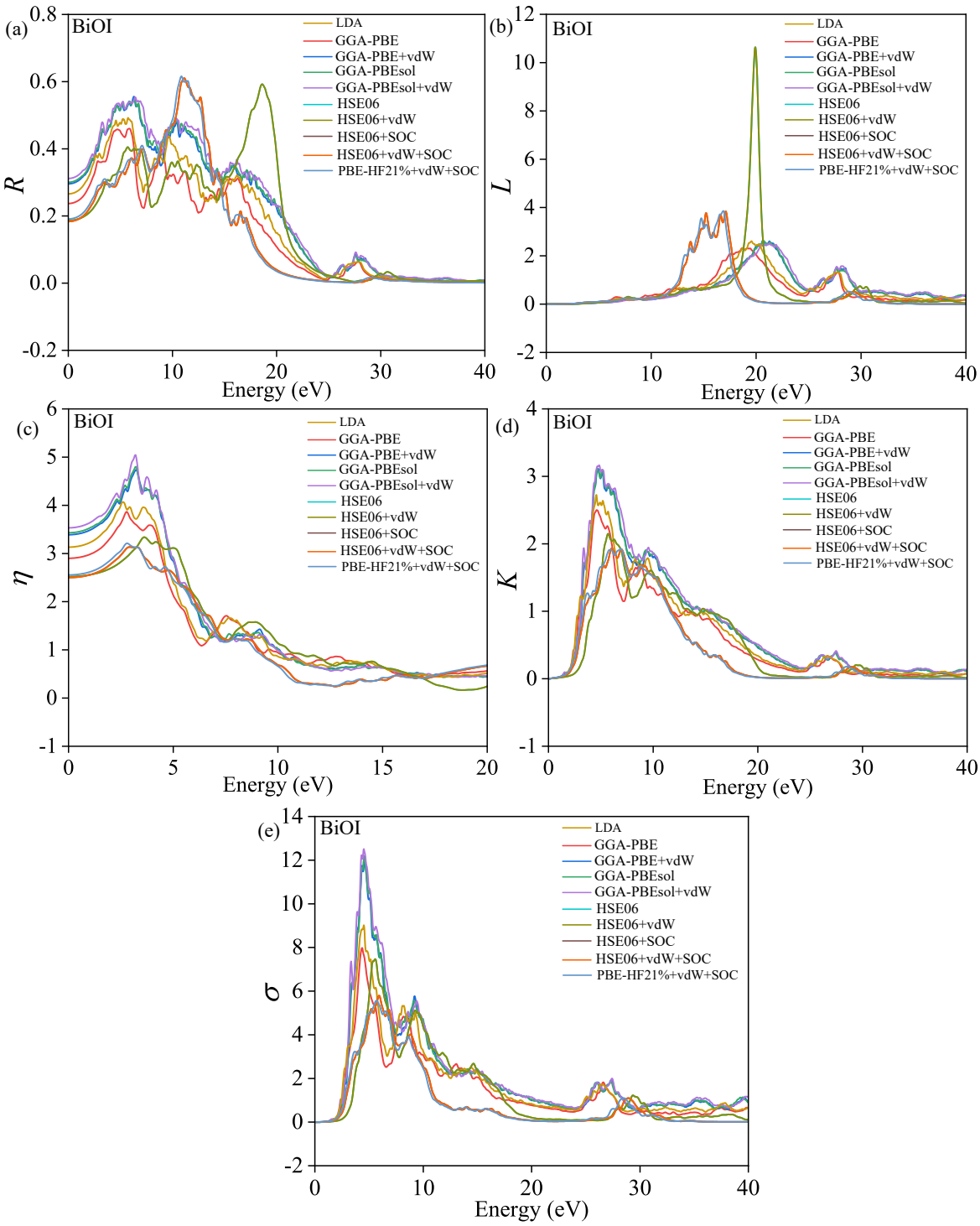

FIG. S17. Linear optical properties: (a) reflectance (R), (b) loss function (L), (c) refractive index (η), (d) extinction coefficient (K), and (e) optical conductivity (σ) of BiOI for different XCFs.

XIV. ELECTRONIC PROPERTIES

TABLE S17. Electronic band gap E_g estimation of BiOX (X = Cl, Br, and I) estimated from density of states (DOS) and band structure (BS) for different XCFs.

Electronic Band Gap Analysis									
	E_g (eV) of BiOCl			E_g (eV) of BiOBr			E_g (eV) of BiOI		
Functional	Exp.	DOS	BS	Exp.	DOS	BS	Exp.	DOS	BS
	3.54	–	–	2.83	–	–	1.85	–	–
LDA	–	2.39	2.54	–	1.85	2.01	–	1.21	1.39
GGA-PBE	–	2.44	2.60	–	2.15	2.33	–	0.87	1.51
GGA-PBE+vdW	–	2.51	2.65	–	1.98	2.17	–	1.04	1.17
GGA-PBEsol	–	2.37	2.52	–	1.94	2.11	–	0.87	0.98
GGA-PBEsol+vdW	–	2.44	2.60	–	1.86	2.04	–	1.02	1.18
GGA-PBE+$U_d + U_p$	–	3.37	3.53	–	2.66	2.85	–	1.67	1.83
HSE06	–	3.39	3.60	–	3.01	3.26	–	2.07	2.29
HSE06+vdW	–	3.39	3.60	–	3.03	3.26	–	2.07	2.29
HSE06+SOC	–	3.15	3.36	–	2.74	2.98	–	1.73	1.95
HSE06+vdW+SOC	–	3.14	3.36	–	2.76	2.98	–	1.72	1.95
PBE-HF30%+vdW+SOC	–	3.41	3.56	–	–	–	–	–	–
PBE-HF22%+vdW+SOC	–	–	–	–	2.69	2.86	–	–	–
PBE-HF21%+vdW+SOC	–	–	–	–	–	–	–	1.61	1.82

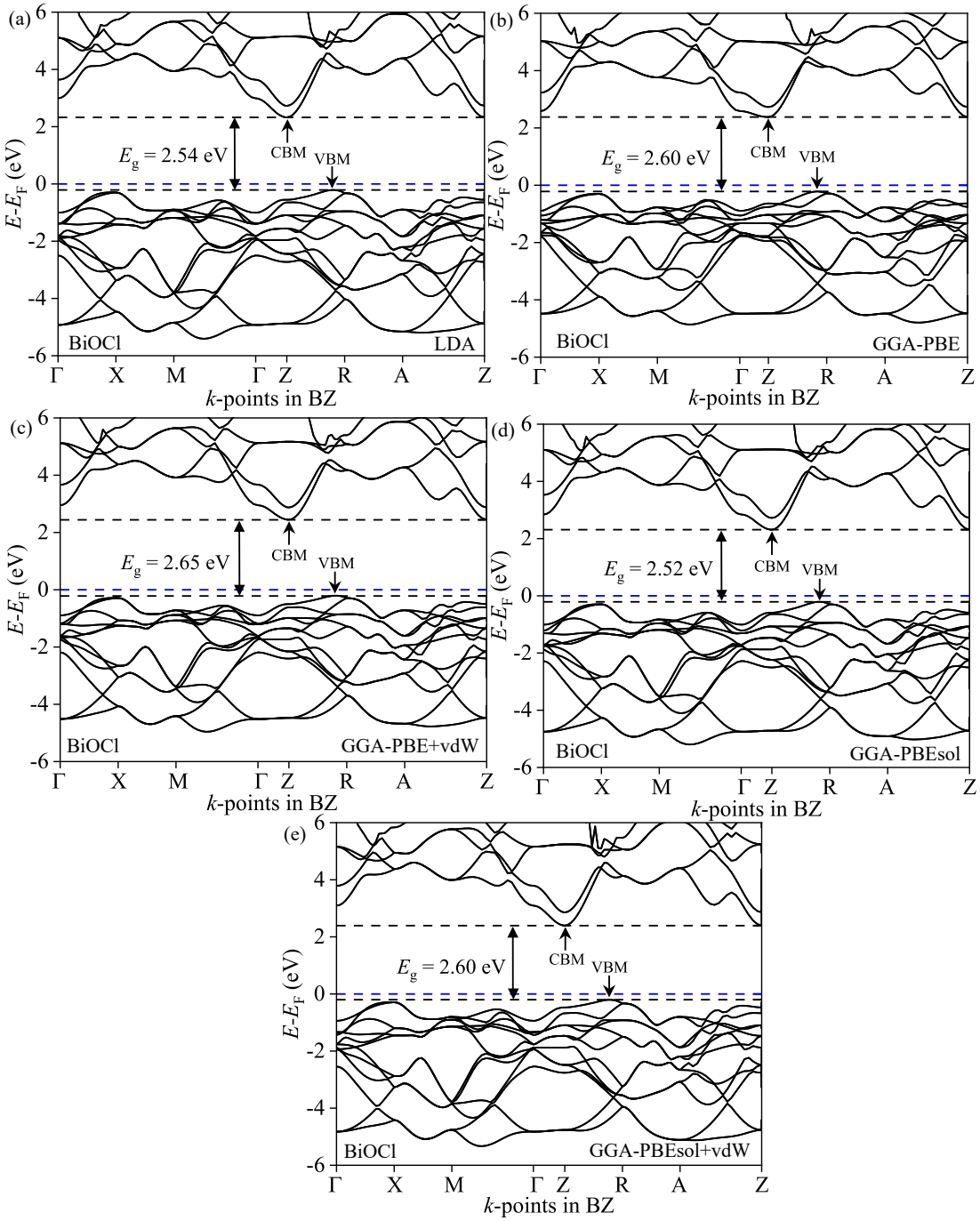

FIG. S18. Electronic BS of cubic BiOCl along A, Γ, M, R, X, and Z high symmetry points in BZ for (a) LDA, (b) GGA-PBE, (c) GGA-PBE+vdW, (d) GGA-PBEsol, and (e) GGA-PBEsol+vdW XCFs.

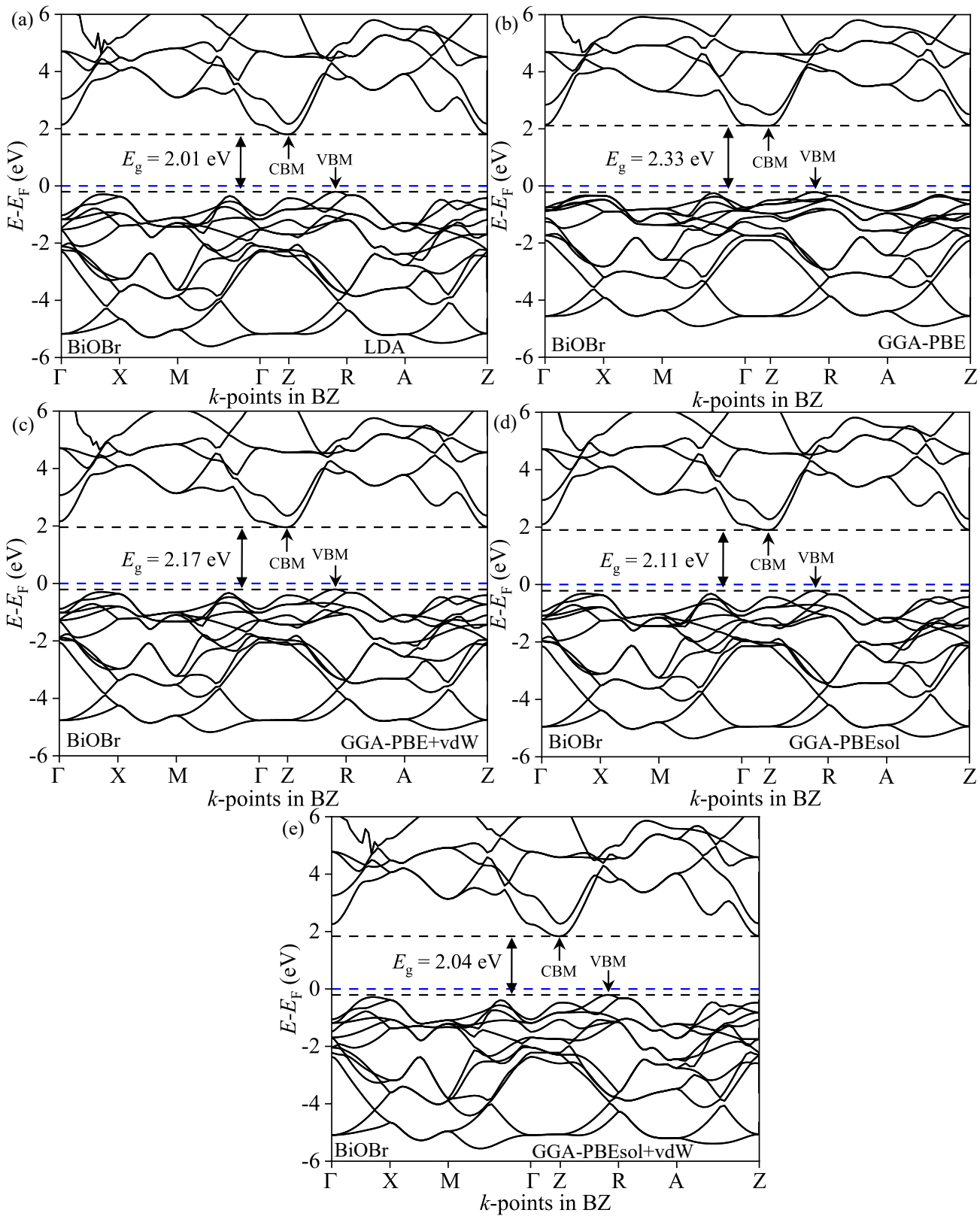

FIG. S19. Electronic BS of cubic BiOBr along A, Γ, M, R, X, and Z high symmetry points in BZ for (a) LDA, (b) GGA-PBE, (c) GGA-PBE+vdW, (d) GGA-PBEsol, and (e) GGA-PBEsol+vdW XCFs.

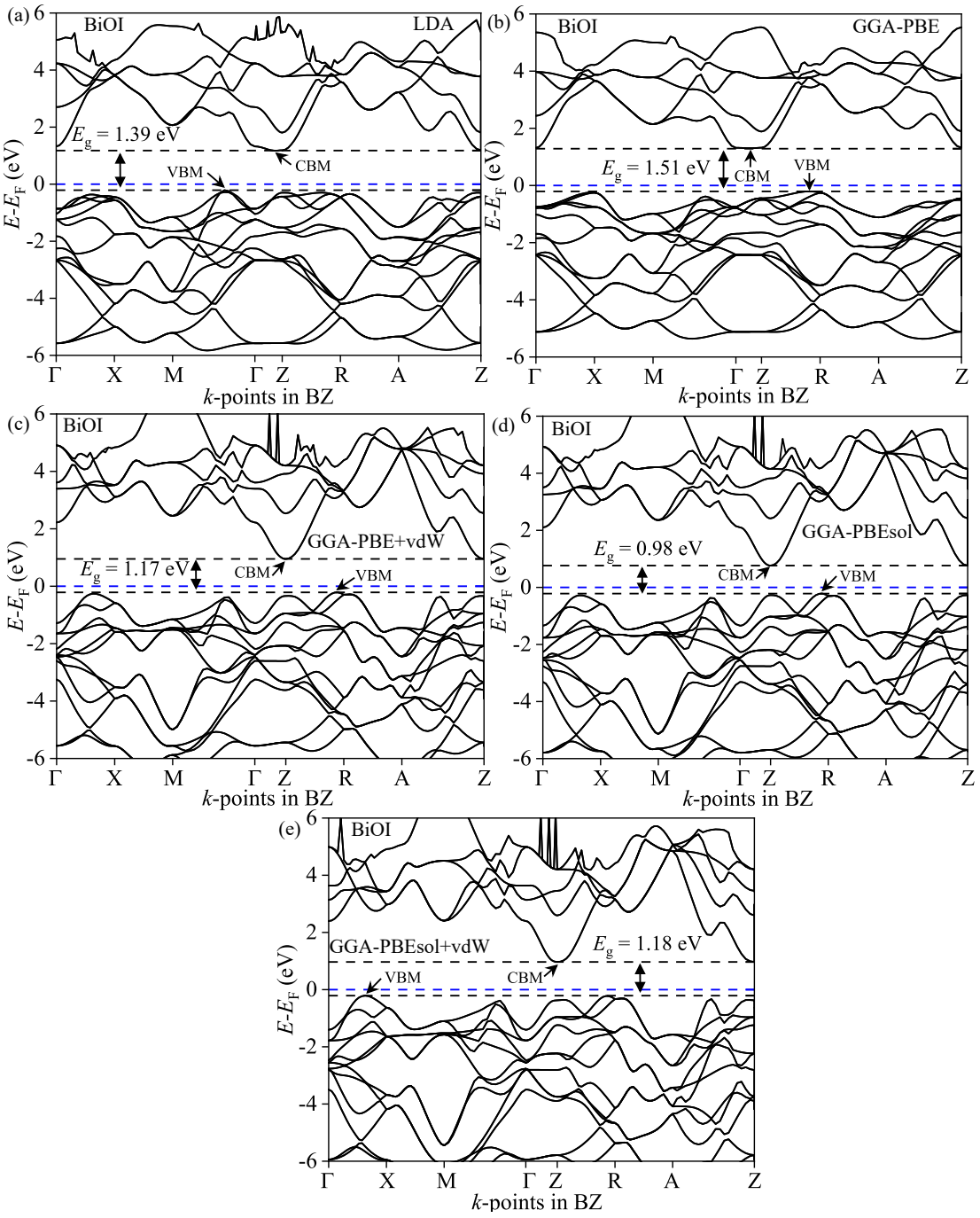

FIG. S20. Electronic BS of cubic BiOI along A, Γ, M, R, X, and Z high symmetry points in BZ for (a) LDA, (b) GGA-PBE, (c) GGA-PBE+vdW (d) GGA-PBEsol, and (e) GGA-PBEsol+vdW XCFs.

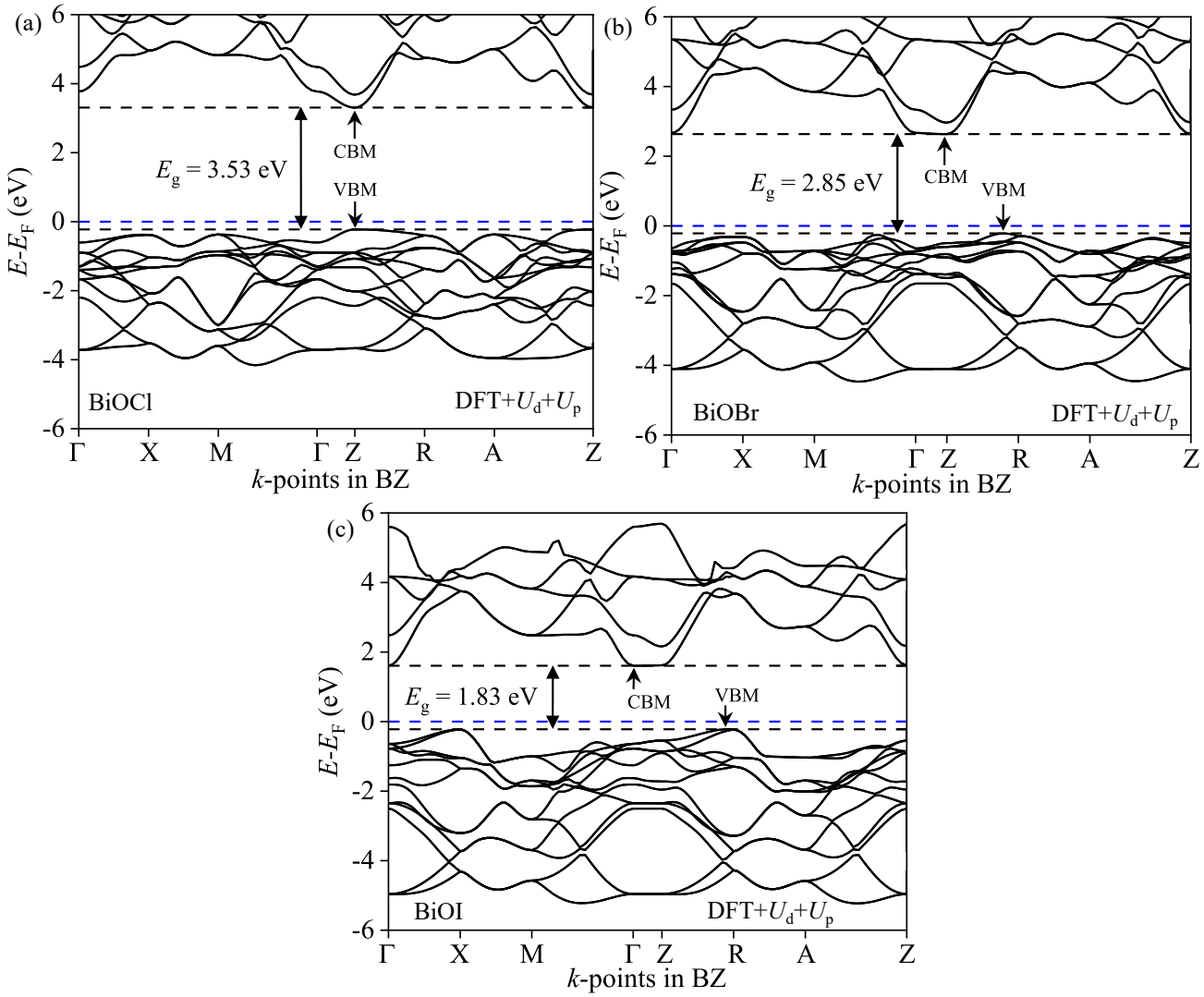

FIG. S21. Electronic BS of (a) BiOCl, (b) BiOBr, and (c) BiOI along A, Γ, M, R, X, and Z high symmetry points in BZ for DFT+U_d+U_p XCF.

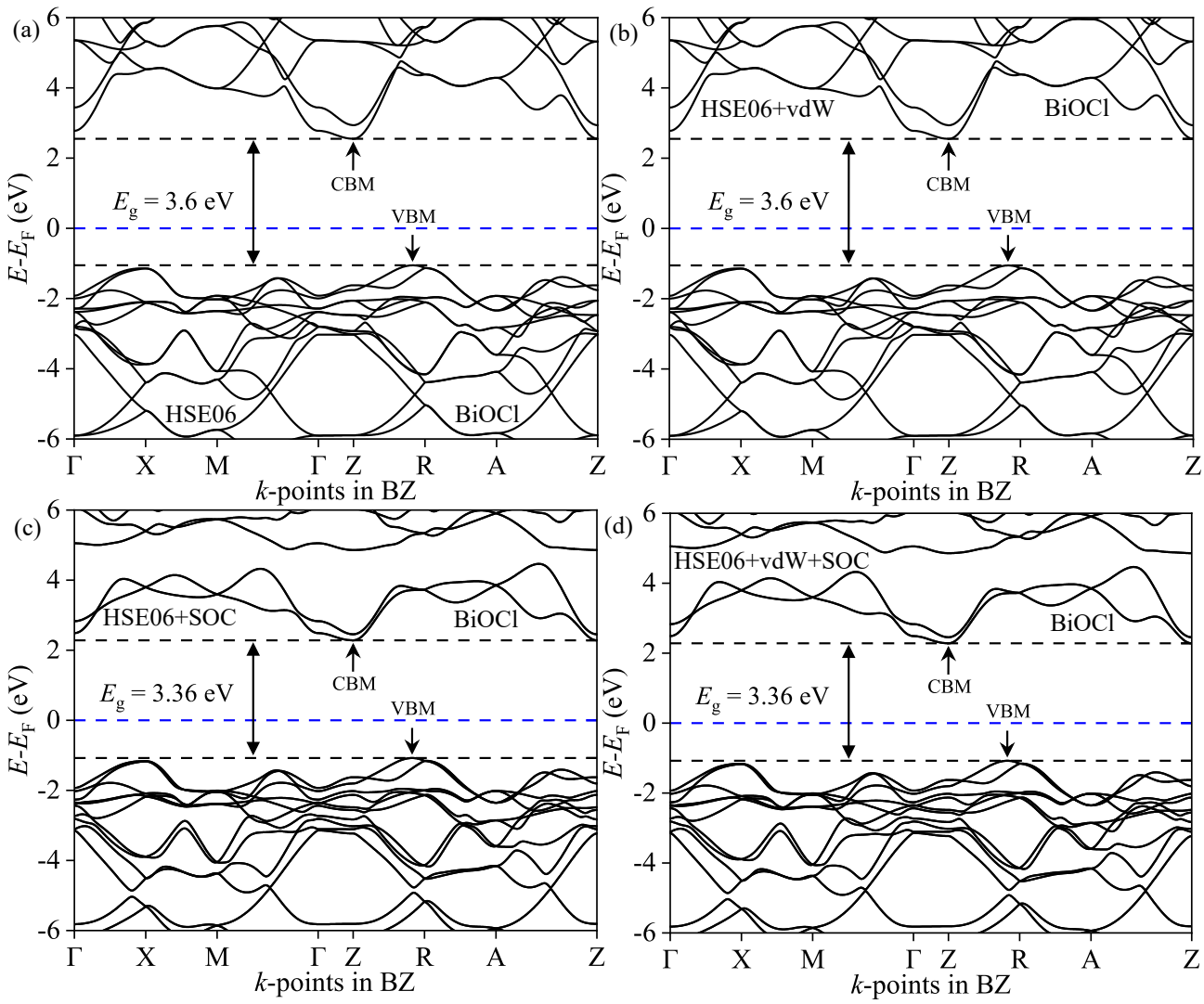

FIG. S22. Electronic BS of cubic BiOCl along A, Γ, M, R, X, and Z high symmetry points in BZ for (a) HSE06, (b) HSE06+vdW, (c) HSE06+SOC, and (d) HSE06+vdW+SOC XCFs.

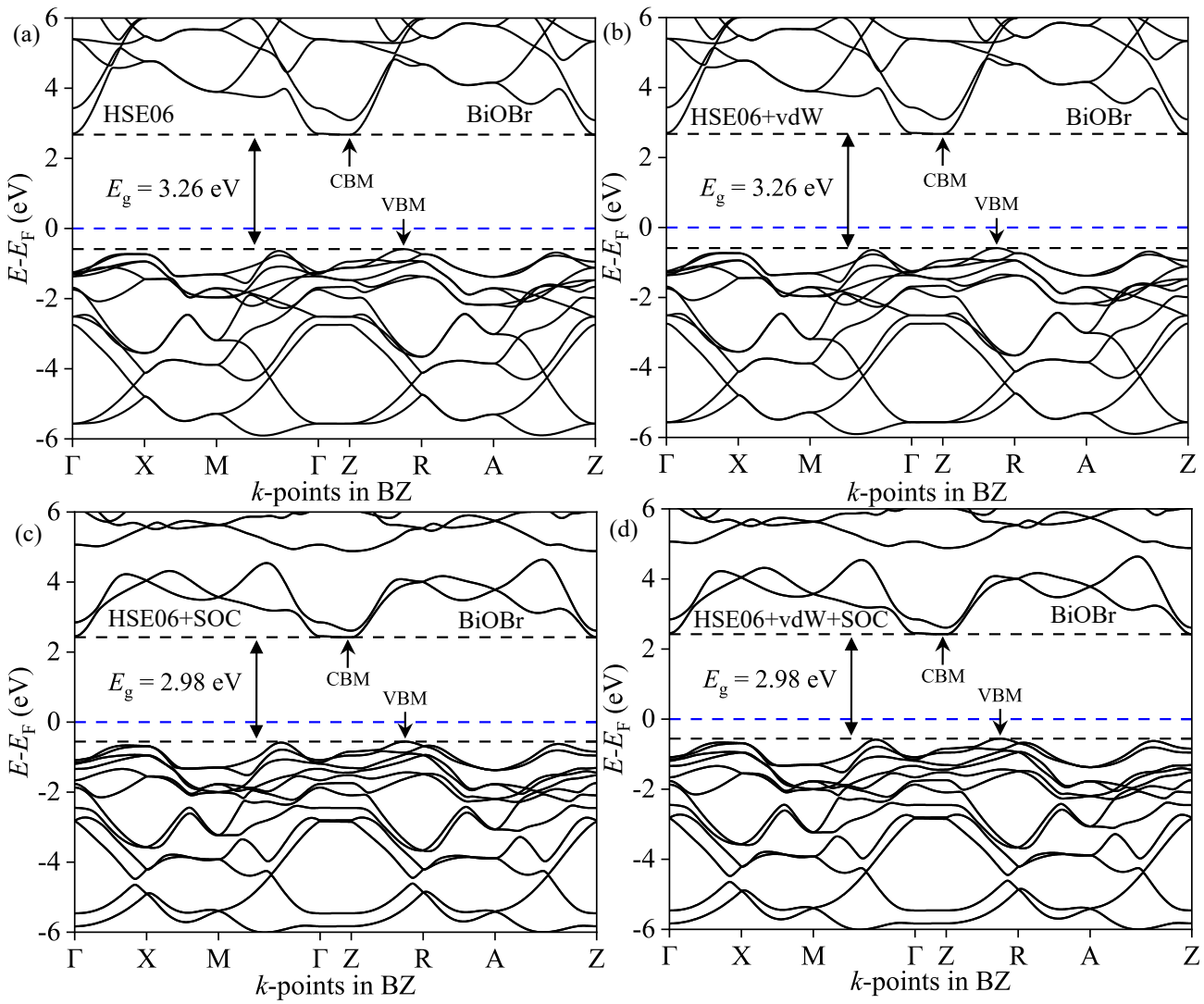

FIG. S23. Electronic BS of cubic BiOBr along A, Γ, M, R, X, and Z high symmetry points in BZ for (a) HSE06, (b) HSE06+vdW, (c) HSE06+SOC, and (d) HSE06+vdW+SOC XCFs.

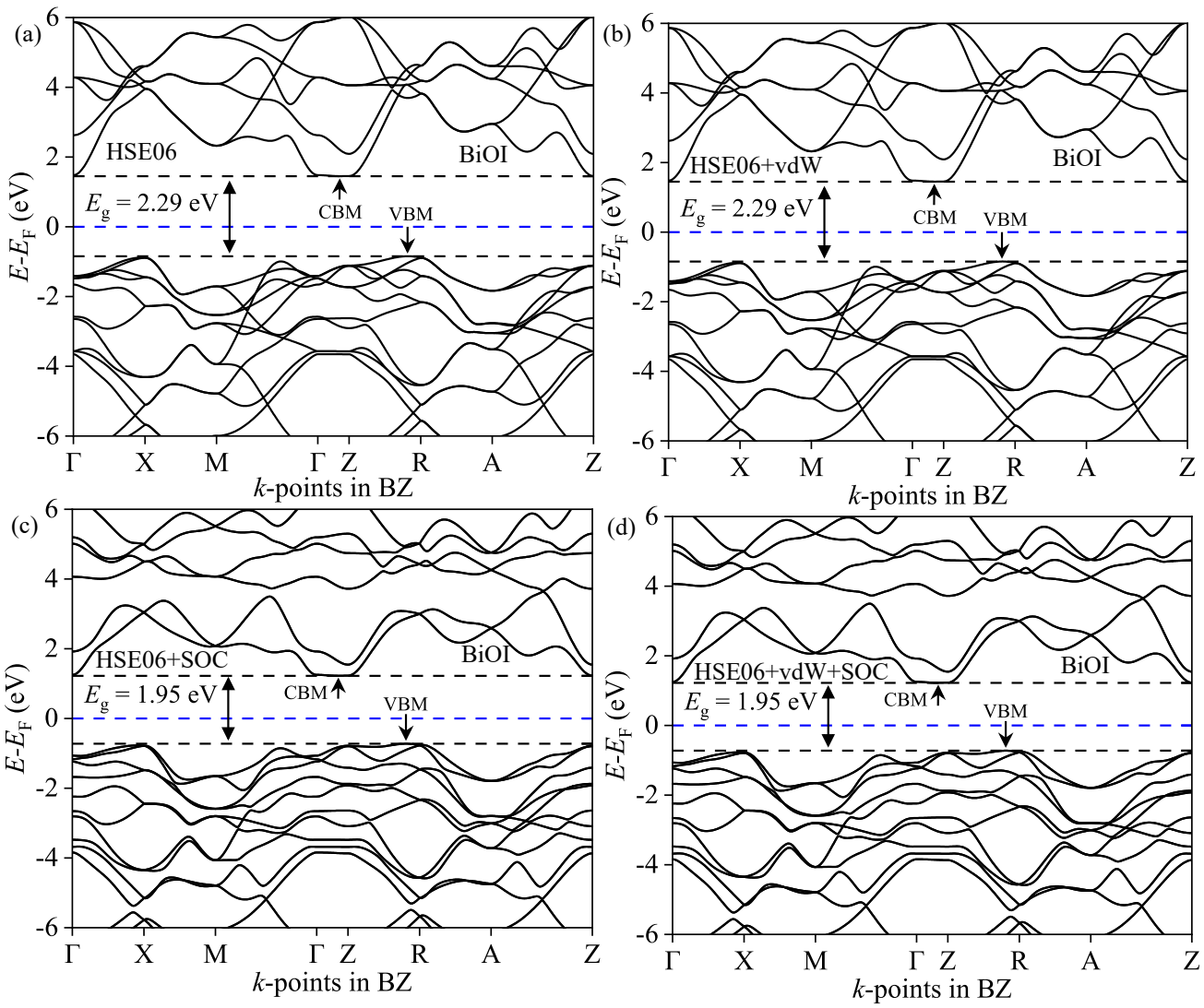

FIG. S24. Electronic BS of cubic BiOI along A, Γ, M, R, X, and Z high symmetry points in BZ for (a) HSE06, (b) HSE06+vdW, (c) HSE06+SOC, and (d) HSE06+vdW+SOC XCFs.

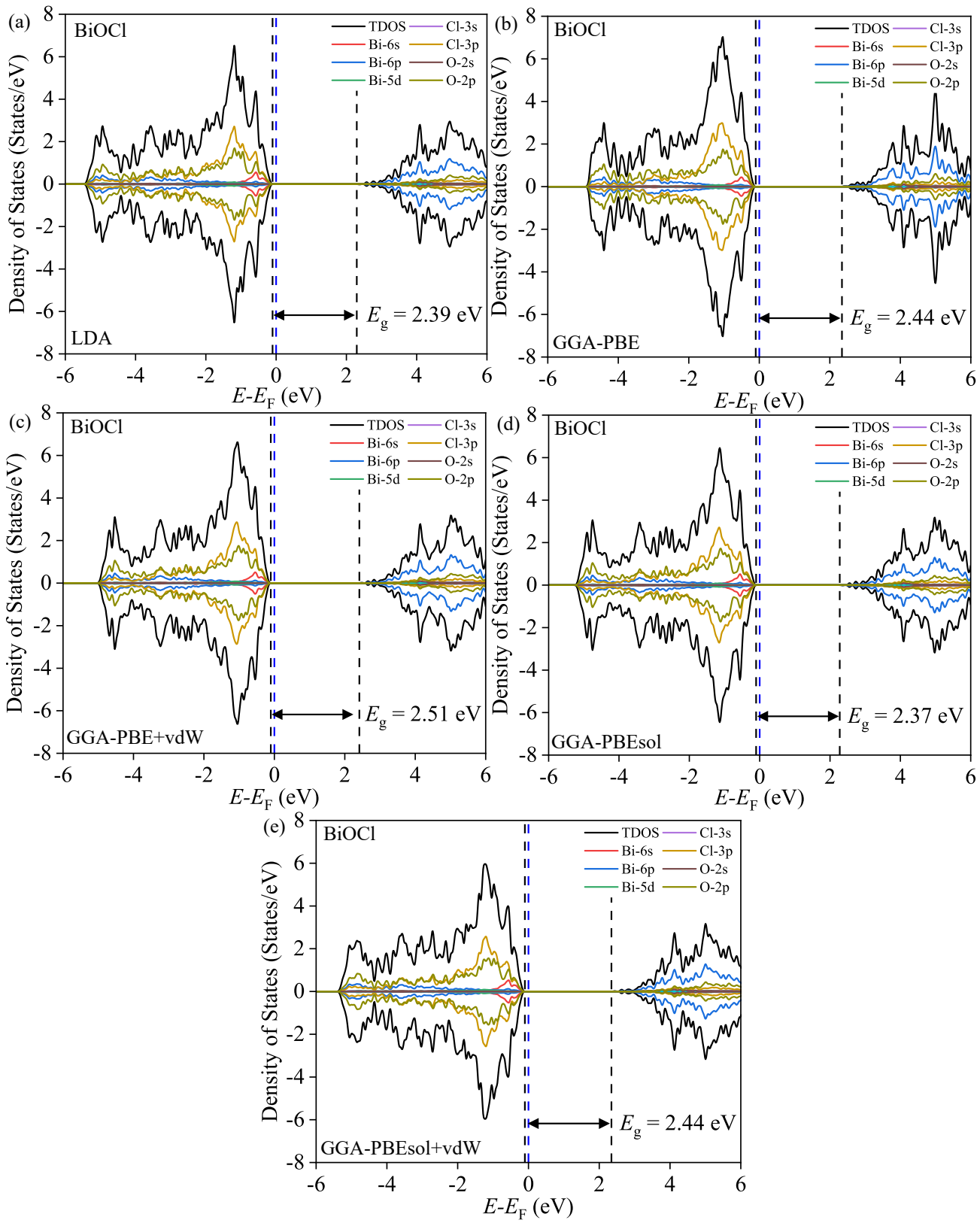

FIG. S25. Total density of states (TDOS) and its projections on different orbitals of Bi, O, and Cl of BiOCl for (a) LDA, (b) GGA-PBE, (c) GGA-PBE+vdW, (d) GGA-PBEsol, and (e) GGA-PBEsol+vdW XCFs.

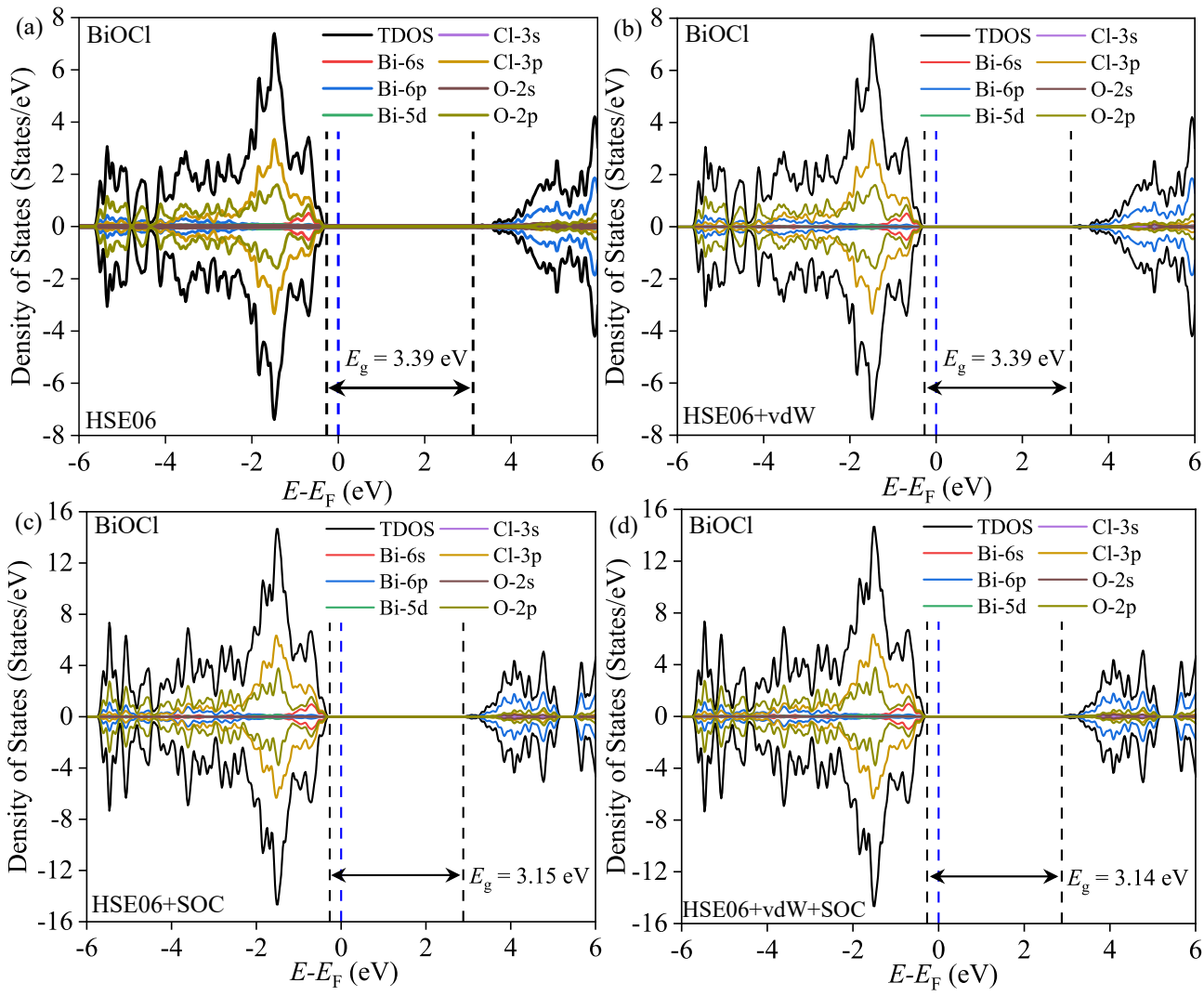

FIG. S26. Total density of states (TDOS) and its projections on different orbitals of Bi, O, and Cl of BiOCl for (a) HSE06, (b) HSE06+vdW, (c) HSE06+SOC, (d) HSE06+vdW+SOC XCFs.

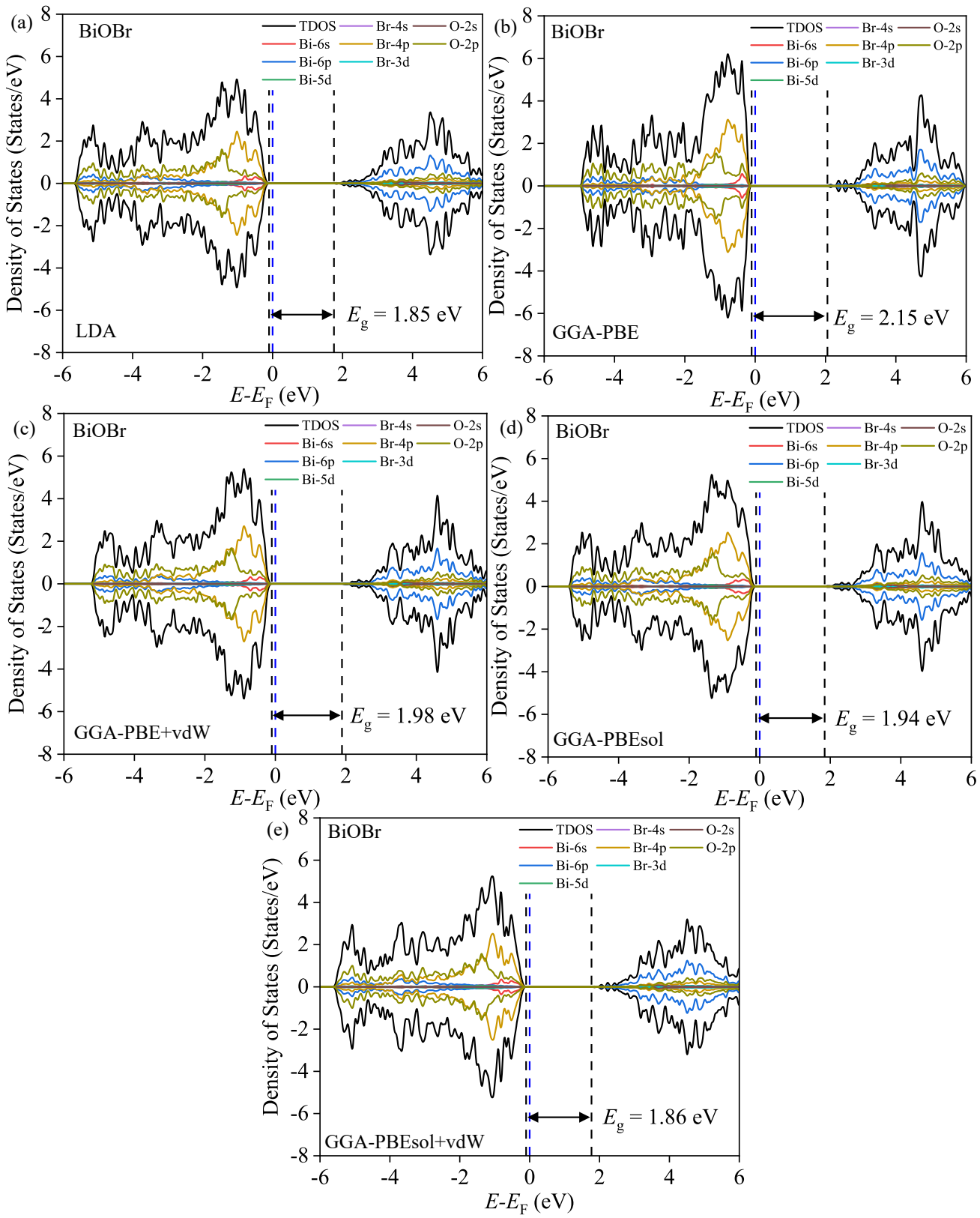

FIG. S27. TDOS and its projections on different orbitals of Bi, O, and Br of BiOBr for (a) LDA, (b) GGA-PBE, (c) GGA-PBE+vdW, (d) GGA-PBEsol, and (e) GGA-PBEsol+vdW XCFs.

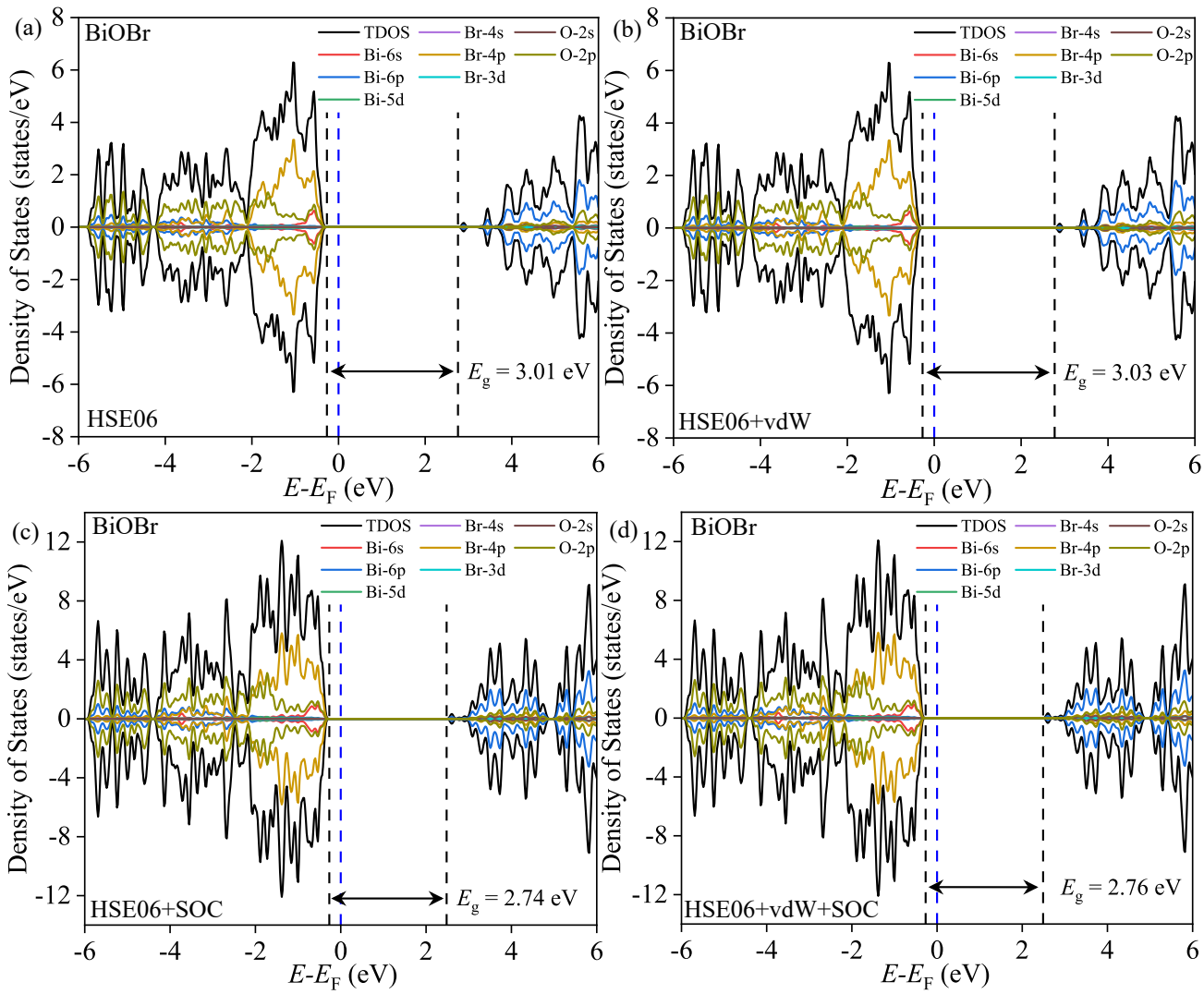

FIG. S28. TDOS and its projections on different orbitals of Bi, O, and Br of BiOBr for (a) HSE06, (b) HSE06+vdW, (c) HSE06+SOC, and (d) HSE06+vdW+SOC.

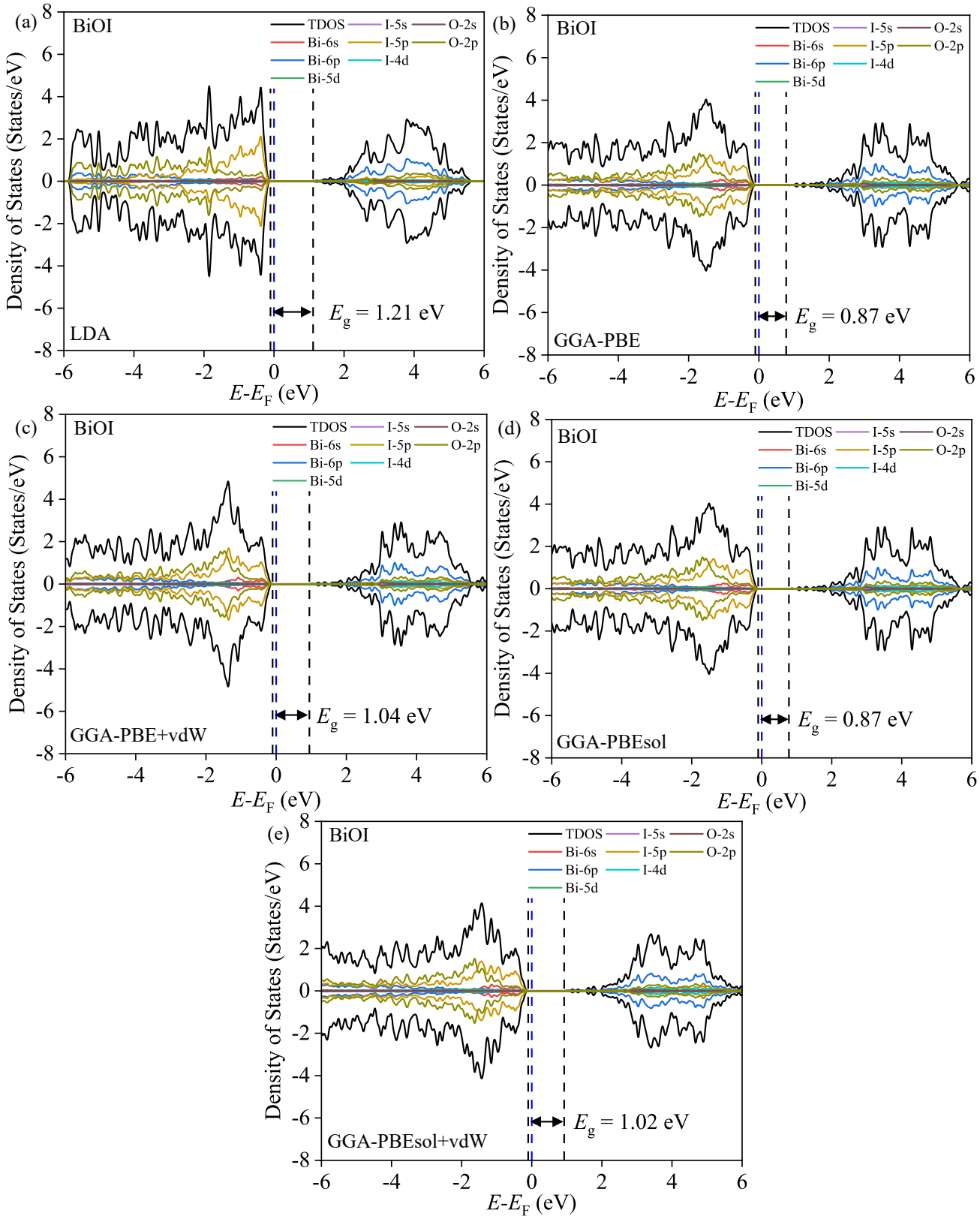

FIG. S29. TDOS and its projections on different orbitals of Bi, O, and I of BiOI for (a) LDA, (b) GGA-PBE, (c) GGA-PBE+vdW, (d) GGA-PBEsol, and (e) GGA-PBEsol+vdW XCFs.

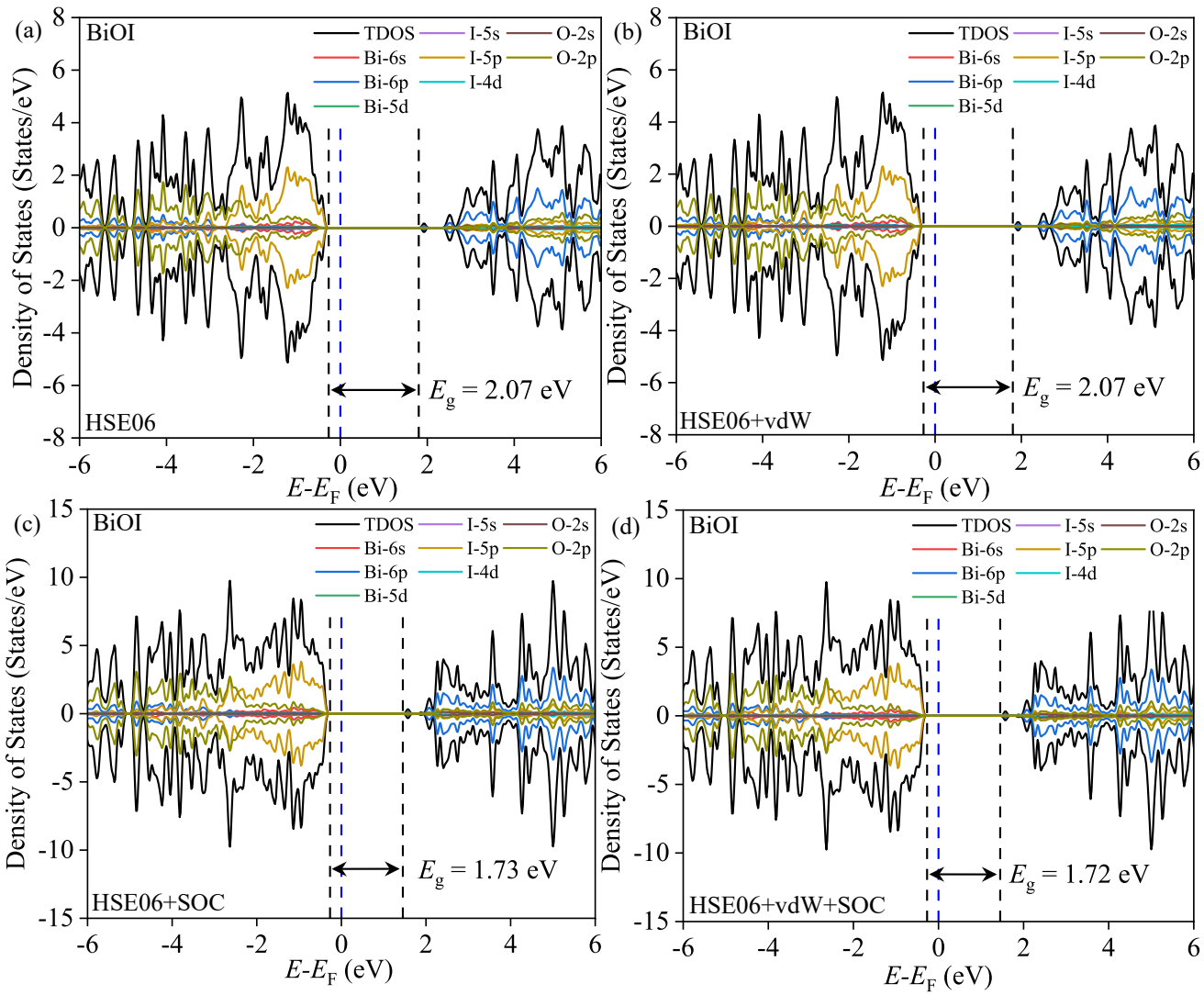

FIG. S30. TDOS and its projections on different orbitals of Bi, O, and I of BiOI for (a) LDA, (b) GGA-PBE, (c) GGA-PBE+vdW, (d) GGA-PBEsol, and (e) GGA-PBEsol+vdW XCFs.

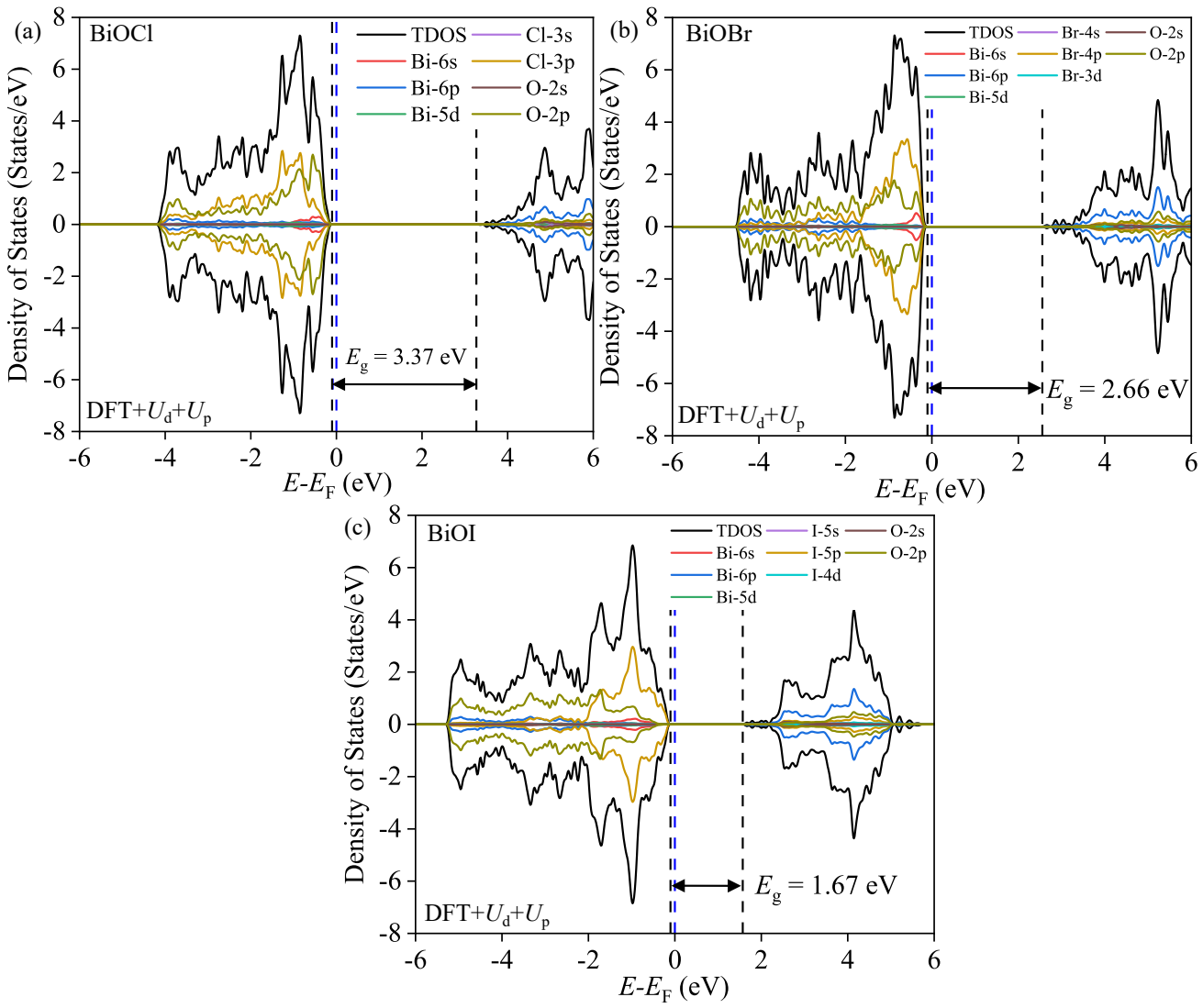

FIG. S31. TDOS and its projections on different orbitals of Bi, O, and X of (a) BiOCl, (b) BiOBr, and (c) BiOI for DFT+U_d+U_p XCF.

XV. EFFECTIVE MASS ANALYSIS

TABLE S18. Effective masses m^*_{xx}, m^*_{yy}, and m^*_{zz} of electron and hole in the units of free electron mass m_0 along different spatial x, y, and z directions of BiOX (X = Cl, Be, and I) for different functionals.

Effective mass analysis								
BiOCl								
	Elctron				Hole			
Functional	m^*_{xx}/m_0	m^*_{yy}/m_0	m^*_{zz}/m_0	Avg.	m^*_{xx}/m_0	m^*_{yy}/m_0	m^*_{zz}/m_0	Avg.
LDA	0.26	0.26	0.44	0.32	0.80	0.80	2.74	1.45
GGA-PBE	0.25	0.25	1.44	0.65	0.86	0.86	2.97	1.56
GGA-PBE+vdW	0.27	0.27	0.61	0.38	0.94	0.94	3.22	1.70
GGA-PBEsol	0.25	0.25	0.55	0.35	0.84	0.84	2.78	1.48
GGA-PBEsol+vdW	0.26	0.26	0.42	0.32	0.85	0.85	2.54	1.41
PBE-HF30%+vdW+SOC	0.22	0.22	1.14	0.53	0.81	0.81	2.98	1.53
BiOBr								
	Elctron				Hole			
Functional	m^*_{xx}/m_0	m^*_{yy}/m_0	m^*_{zz}/m_0	Avg.	m^*_{xx}/m_0	m^*_{yy}/m_0	m^*_{zz}/m_0	Avg.
LDA	0.22	0.22	1.06	0.50	0.68	0.68	1.72	1.02
GGA-PBE	0.23	0.23	3.5	1.32	1.25	1.25	3.04	1.85
GGA-PBE+vdW	0.23	0.23	1.80	0.75	0.88	0.88	2.16	1.31
GGA-PBEsol	0.20	0.20	1.70	0.70	0.76	0.76	1.85	1.12
GGA-PBEsol+vdW	0.24	0.24	0.92	0.47	0.69	0.69	1.72	1.03
PBE-HF22%+vdW+SOC	0.19	0.19	8.78	3.05	1.14	1.14	7.48	3.26
BiOI								
	Elctron				Hole			
Functional	m^*_{xx}/m_0	m^*_{yy}/m_0	m^*_{zz}/m_0	Avg.	m^*_{xx}/m_0	m^*_{yy}/m_0	m^*_{zz}/m_0	Avg.
LDA	0.19	0.19	1.84	0.75	0.52	0.52	0.70	0.58
GGA-PBE	0.16	0.16	1.04	0.46	0.58	0.58	2.04	1.06
GGA-PBE+vdW	0.30	0.30	0.24	0.28	0.57	0.57	0.61	0.58
GGA-PBEsol	0.25	0.25	0.21	0.24	0.52	0.52	0.54	0.52
GGA-PBEsol+vdW	0.43	0.43	0.26	0.37	0.47	0.47	0.57	0.50
PBE-HF21%+vdW+SOC	0.17	0.17	5.64	1.99	0.83	0.83	3.24	1.67

XVI. CARRIER TRANSPORT

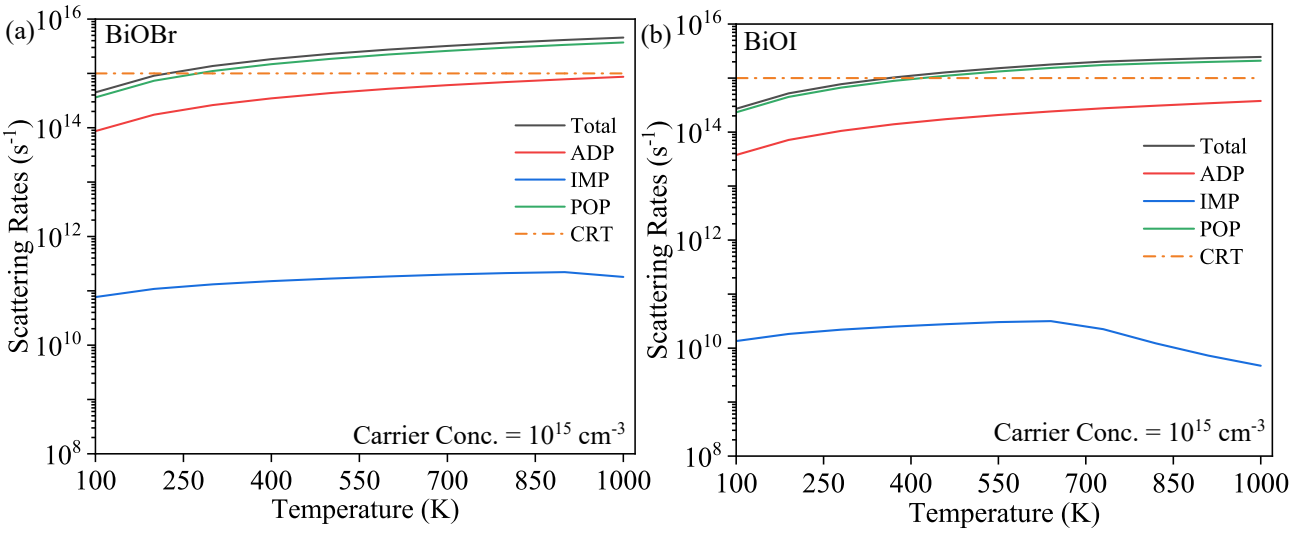

FIG. S32. Average temperature-dependent scattering rates of (a) BiOBr, and (b) BiOI for IMP, ADP, POP, and CRT. Scattering rates are averaged over k-points in BZ and Fermi-Dirac distribution derivatives.

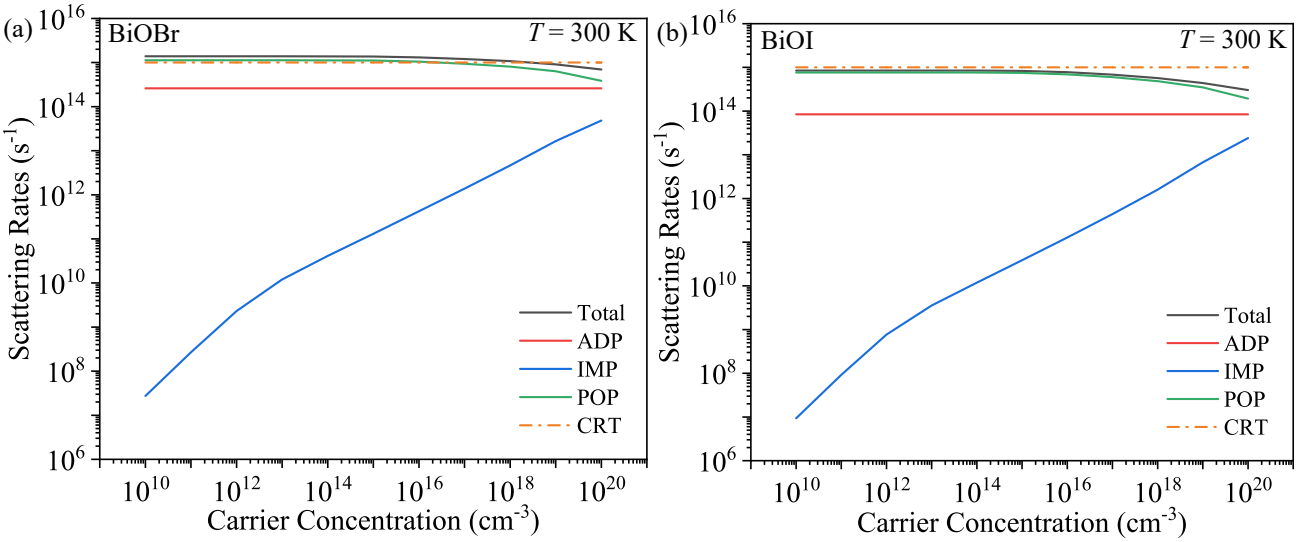

FIG. S33. Average carrier concentration-dependent scattering rates of (a) BiOBr, and (b) BiOI for IMP, ADP, POP, and CRT. Scattering rates are averaged over k-points in BZ and Fermi-Dirac distribution derivatives.

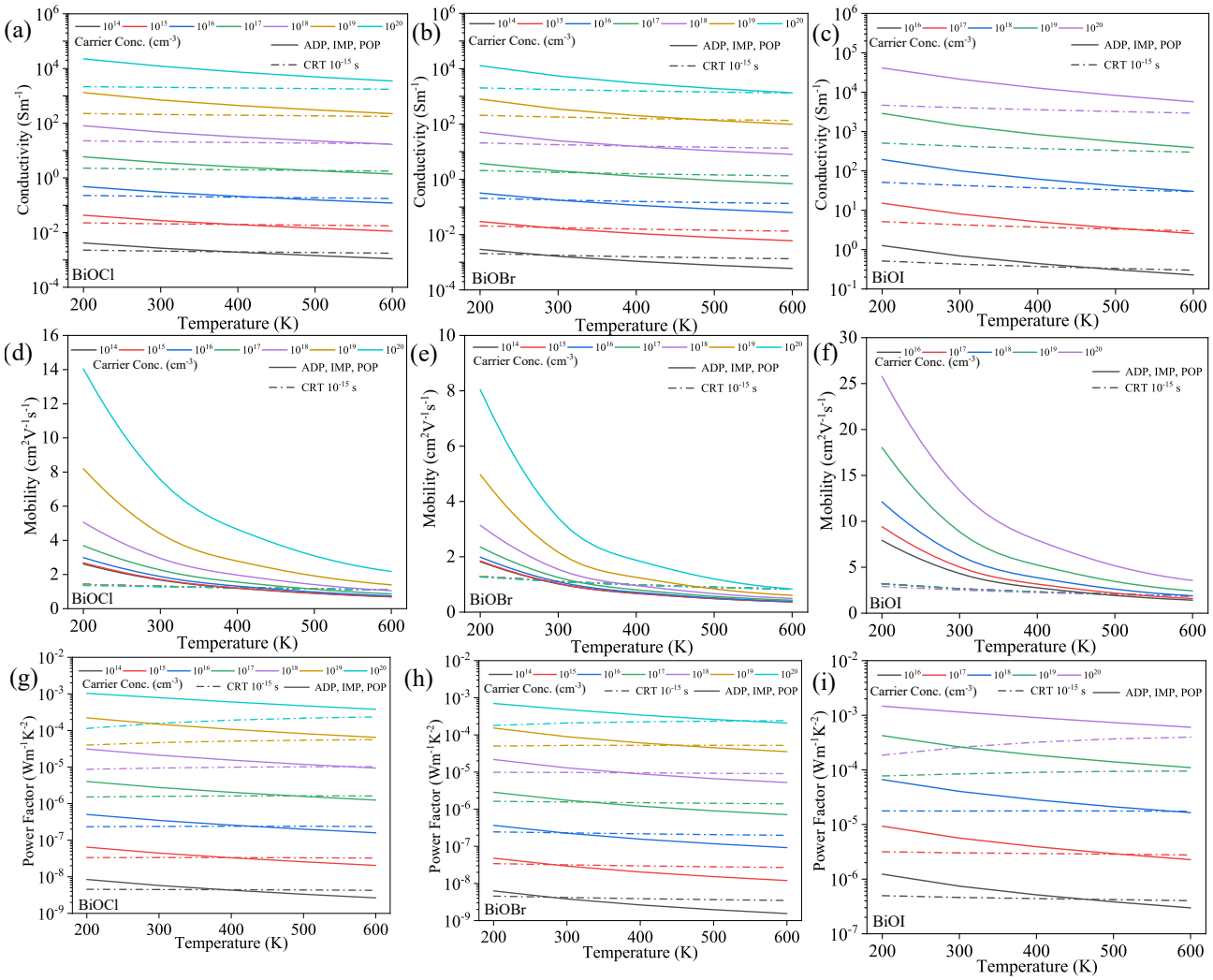

FIG. S34. Spatially averaged p-type conductivity (σ) of (a) BiOCl, (b) BiOBr, and (c) BiOI; mobility (μ) of (d) BiOCl, (e) BiOBr, and (f) BiOI; power factor ($S^2\sigma$) of (g) BiOCl, (h) BiOBr, and (i) BiOI as a function of temperature for different carrier concentrations.

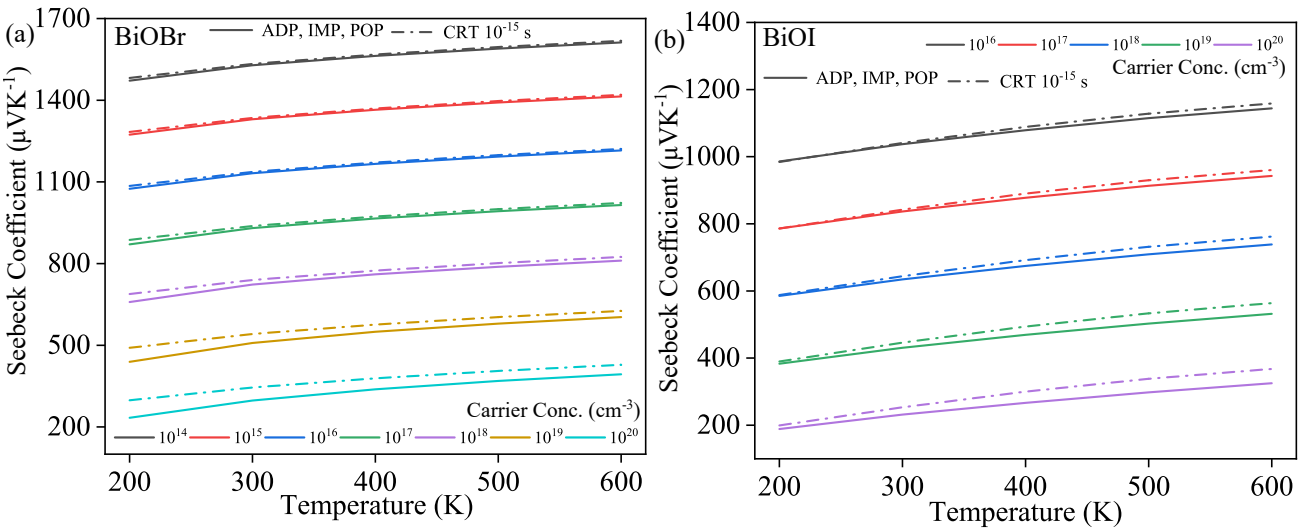

FIG. S35. Spatially averaged Seebeck coefficient (S) of (a) BiOBr, and (b) BiOI as a function of temperature for different carrier concentrations.

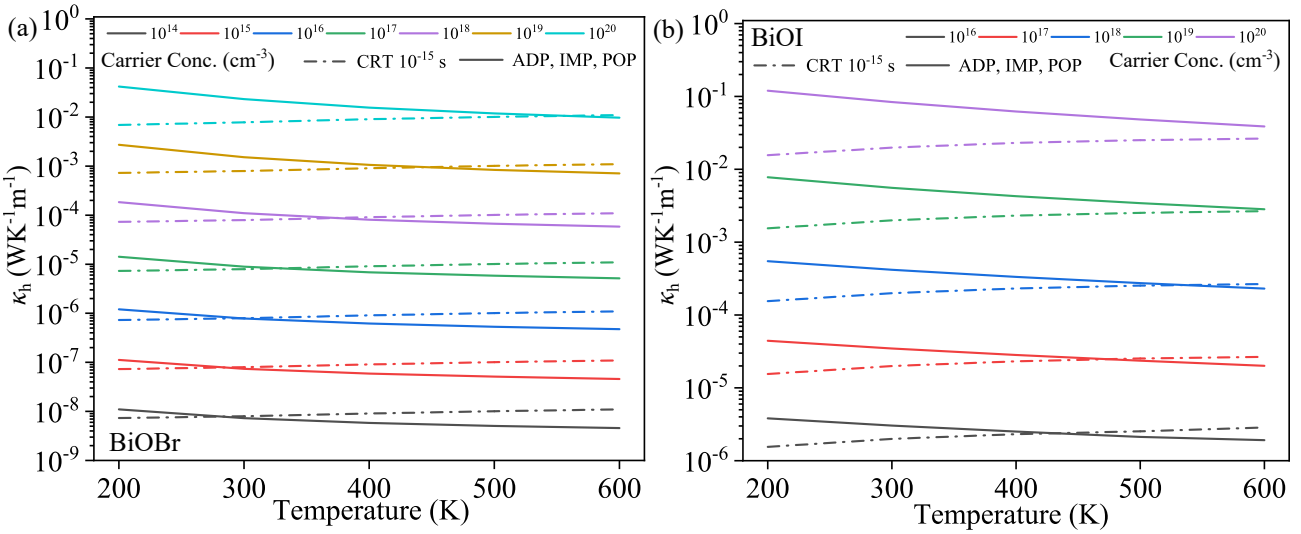

FIG. S36. Spatially averaged electronic contribution to thermal conductivity (κ_{h}) of (a) BiOBr, and (b) BiOI as a function of temperature for different carrier concentrations.

XVII. ELECTRONIC BAND-EDGE ANALYSIS

TABLE S19. Experimental (Exp.) and DFT (DFT+U_d+U_p, HSE06, HSE06+vdW+SOC, and PBE-HFα_{HF}%+vdW+SOC XCFs) simulated electronic band edges E_{VBM} and E_{CBM} of BiOX (X = Cl, Br, I), calculated from Mullikan electronegativity χ, band gap E_g, and free energy of electron E_e.

Electronic Band-edge Analysis					
BiOCl/DFT	χ (eV)	E_g (eV)	E_e (eV)	E_{VBM} (eV)	E_{CBM} (eV)
Exp.	6.43	3.54	4.44	0.04	3.57
GGA-PBE+U_d + U_p	6.43	3.53	4.44	0.04	3.57
HSE06	6.43	3.60	4.44	0.00	3.60
HSE06+vdW+SOC	6.43	3.36	4.44	0.12	3.48
PBE-HF30%+vdW+SOC	6.43	3.56	4.44	0.02	3.58
BiOBr/DFT					
Exp.	6.24	2.83	4.44	0.39	3.22
GGA-PBE+U_d + U_p	6.24	2.85	4.44	0.38	3.23
HSE06	6.24	3.26	4.44	0.17	3.43
HSE06+vdW+SOC	6.24	2.98	4.44	0.31	3.29
PBE-HF22%+vdW+SOC	6.24	2.86	4.44	0.37	3.23
BiOI/DFT					
Exp.	6.01	1.83	4.44	0.89	2.72
GGA-PBE+U_d + U_p	6.01	2.83	4.44	0.89	2.72
HSE06	6.01	2.29	4.44	0.66	2.95
HSE06+vdW+SOC	6.01	1.95	4.44	0.83	2.78
PBE-HF21%+vdW+SOC	6.01	1.82	4.44	0.89	2.71

XVIII. REDOX POTENTIAL ANALYSIS

TABLE S20. Redox potential (R.P.) V analysis concerning normal hydrogen electrode (NHE) for relevant photocatalytic reactions.

Redox Potential (R.P.) Analysis			
Reaction	R.P. (pH = 0)	R.P. (pH = 2)	R.P. (pH = 10)
$O_2 + e^- \rightarrow \cdot O_2^-$	−0.18	−0.29	−0.77
$2H^+ + O_2 + 2e^- \rightarrow H_2O_2$	0.695	0.577	0.105
$H_2O_2 + H^+ + e^- \rightarrow \cdot OH^- + H_2O$	0.8	0.68	0.21
$OH^- \rightarrow \cdot OH + e^-$	1.99	1.87	1.4
$H_2O \rightarrow \cdot OH + H^+ + e^-$	2.73	2.61	2.14

[1] G. Kresse and J. Furthmüller, Efficient iterative schemes for ab initio total-energy calculations using a plane-wave basis set, Phys. Rev. B **54**, 11169 (1996).

[2] G. Kresse and D. Joubert, From ultrasoft pseudopotentials to the projector augmented-wave method, Phys. Rev. B **59**, 1758 (1999).

[3] P. E. Blöchl, Projector augmented-wave method, Phys. Rev. B **50**, 17953 (1994).

[4] A. Jain, Y. Shin, and K. A. Persson, Computational predictions of energy materials using density functional theory, Nat. Rev. Mater. **1**, 1 (2016).

[5] R. O. Jones, Density functional theory: Its origins, rise to prominence, and future, Rev. Mod. Phys. **87**, 897 (2015).

[6] D. M. Ceperley and B. J. Alder, Ground state of the electron gas by a stochastic method, Phys. Rev. Lett. **45**, 566 (1980).

[7] J. P. Perdew, K. Burke, and M. Ernzerhof, Generalized gradient approximation made simple, Phys. Rev. Lett. **77**, 3865 (1996).

[8] J. P. Perdew, A. Ruzsinszky, G. I. Csonka, O. A. Vydrov, G. E. Scuseria, L. A. Constantin, X. Zhou, and K. Burke, Restoring the density-gradient expansion for exchange in solids and surfaces, Phys. Rev. Lett. **100**, 136406 (2008).

[9] S. Dudarev, G. Botton, S. Savrasov, C. Humphreys, and A. Sutton, Electron-energy-loss spectra and the structural stability of nickel oxide: An LSDA+U study, Phys. Rev. B **57**, 1505 (1998).

[10] O. Volnianska, P. Boguslawski, J. Kaczkowski, P. Jakubas, A. Jezierski, and E. Kaminska, Theory of doping properties of Ag acceptors in ZnO, Phys. Rev. B **80**, 245212 (2009).

[11] R. M. Sheetz, I. Ponomareva, E. Richter, A. N. Andriotis, and M. Menon, Defect-induced optical absorption in the visible range in ZnO nanowires, Phys. Rev. B **80**, 195314 (2009).

[12] N. N. Lathiotakis, A. N. Andriotis, and M. Menon, Codoping: A possible pathway for inducing ferromagnetism in ZnO, Phys. Rev. B **78**, 193311 (2008).

[13] S.-G. Park, B. Magyari-Köpe, and Y. Nishi, Electronic correlation effects in reduced rutile TiO_2 within the LDA+U method, Phys. Rev. B **82**, 115109 (2010).

[14] S. Grimme, S. Ehrlich, and L. Goerigk, Effect of the damping function in dispersion corrected density functional theory, J. Comput. Chem. **32**, 1456 (2011).

[15] J. Heyd, G. E. Scuseria, and M. Ernzerhof, Hybrid functionals based on a screened Coulomb potential, J. Chem. Phys. **118**, 8207 (2003).

[16] M. Z. Hossain, S. S. Nishat, S. Ahmed, Q. S. Hossain, M. N. Khan, T. Hasan, M. S. Bashar, A. S. H. Faysal, I. M. Syed, K. S. Hossain, *et al.*, Combined experimental and DFT approach to $BiNbO_4$ polymorphs, RSC Adv. **13**, 5576 (2023).

[17] J. Fardush Tanha, S. Farhad, U. Honey, N. Tanvir, T. Hasan, S. Shahriyar Nishat, A. Kabir, S. Ahmed, M. Hakim, M. N. I. Khan, *et al.*, A DFT+U look into experimentally synthesized monoclinic scheelite $BiVO_4$, J. Appl. Phys. **130**, 235107 (2021).

[18] T. Le Bahers, M. Rerat, and P. Sautet, Semiconductors used in photovoltaic and photocatalytic devices: Assessing fundamental properties from DFT, J. Phys. Chem. C **118**, 5997 (2014).

[19] C. Franchini, Hybrid functionals applied to perovskites, J. Phys. Condens. Matter. **26**, 253202 (2014).

[20] A. Stroppa and G. Kresse, Unraveling the Jahn-Teller effect in Mn-doped GaN using the Heyd-Scuseria-Ernzerhof hybrid functional, Phys. Rev. B **79**, 201201 (2009).

[21] A. Stroppa and S. Picozzi, Hybrid functional study of proper and improper multiferroics, Phys. Chem. Chem. Phys. **12**, 5405 (2010).

[22] M. Marsman, J. Paier, A. Stroppa, and G. Kresse, Hybrid functionals applied to extended systems, J. Phys. Condens. Matter. **20**, 064201 (2008).

[23] K. E. Kweon and G. S. Hwang, Structural phase-dependent hole localization and transport in bismuth vanadate, Phys. Rev. B **87**, 205202 (2013).

[24] L. Schimka, J. Harl, and G. Kresse, Improved hybrid functional for solids: The HSEsol functional, J. Chem. Phys. **134** (2011).

[25] Q. S. Hossain, S. Ahmed, S. S. Nishat, M. Z. Hossain, M. N. I. Khan, T. Hasan, M. S. Bashar, M. Hakim, I. M. Syed, K. S. Hossain, *et al.*, An ab initio DFT perspective on experimentally synthesized $CuBi_2O_4$, RSC Adv. **13**, 14291 (2023).

[26] Y.-S. Kim, K. Hummer, and G. Kresse, Accurate band structures and effective masses for InP, InAs, and InSb using hybrid functionals, Phys. Rev. B **80**, 035203 (2009).

[27] G. K. Madsen and D. J. Singh, BoltzTraP. A code for calculating band-structure dependent quantities, Comput. Phys. Commun. **175**, 67 (2006).

[28] A. M. Ganose, J. Park, A. Faghaninia, R. Woods-Robinson, K. A. Persson, and A. Jain, Efficient calculation of carrier scattering rates from first principles, Nat. Commun. **12**, 2222 (2021).

[29] A. Togo and I. Tanaka, First principles phonon calculations in materials science, Scr. Mater. **108**, 1 (2015).

[30] A. Togo, L. Chaput, and I. Tanaka, Distributions of phonon lifetimes in Brillouin zones, Phy. Rev. B **91**, 094306 (2015).

[31] S. Baroni, S. De Gironcoli, A. Dal Corso, and P. Giannozzi, Phonons and related crystal properties from density-functional perturbation theory, Rev. Mod. Phys. **73**, 515 (2001).

[32] F. Giustino, Electron-phonon interactions from first principles, Rev. Mod. Phys. **89**, 015003 (2017).

[33] A. Togo, L. Chaput, T. Tadano, and I. Tanaka, Implementation strategies in phonopy and phono3py, J. Phys. Condens. Matter. (2023).

[34] A. A. Mostofi, J. R. Yates, Y.-S. Lee, I. Souza, D. Vanderbilt, and N. Marzari, wannier90: A tool for obtaining maximally-localised wannier functions, Comput. Phys. Commun. **178**, 685 (2008).

[35] Y. Hou, S. Ardo, and R. Wu, Hybrid density functional study of band gap engineering of $SrTiO_3$ photocatalyst via doping for water splitting, Phys. Rev. Mater. **5**, 065801 (2021).

[36] S. Ahmed, S. S. Nishat, A. Kabir, A. S. H. Faysal, T. Hasan, S. Chakraborty, and I. Ahmed, Structural, elastic, vibrational, electronic and optical properties of $SmFeO_3$ using density functional theory, Physica B Condens. Matter. **615**, 413061 (2021).

[37] P. Giannozzi, S. Baroni, N. Bonini, M. Calandra, R. Car, C. Cavazzoni, D. Ceresoli, G. L. Chiarotti, M. Cococcioni, I. Dabo, *et al.*, QUANTUM ESPRESSO: A modular and open-source software project for quantum simulations of materials, J. Phys.: Condens. Matter. **21**, 395502 (2009).

[38] P. Giannozzi, O. Andreussi, T. Brumme, O. Bunau, M. B. Nardelli, M. Calandra, R. Car, C. Cavazzoni, D. Ceresoli, M. Cococcioni, *et al.*, Advanced capabilities for materials modelling with quantum espresso, J. Phys. Condens. Matter **29**, 465901 (2017).

[39] P. Giannozzi, O. Baseggio, P. Bonfà, D. Brunato, R. Car, I. Carnimeo, C. Cavazzoni, S. De Gironcoli, P. Delugas, F. Ferrari Ruffino, *et al.*, Quantum ESPRESSO toward the exascale, J. Chem. Phys. **152**, 154105 (2020).